Water renewal in a threshold fjord: A simulation study of submerged fresh water discharge

Master's thesis in applied and computational mathematics

Ragnhild Evebø Sand

November 20, 2018

Department of Mathematics
University of Bergen

Acknowledgements

I would like to express my gratitude towards my supervisor, Jarle Berntsen. Your door has always been open, and you are always so positive. If I am stuck at a code, or having questions about hydrodynamics, modelling or my results - you always have an answer and are always eager to help.

I would also like to thank Einar Bye-Ingebrigtsen and Trond Einar Isaksen at UniResearch for providing data material used in this study, and Dag Aksnes for advice regarding the modelling of dissolved oxygen.

I must also thank my beloved family and friends. The fact that you all believe in me and are so supporting is amazing. Håkon, you are my best friend and have been such a great support, especially in these final months and in moments where I have doubted in myself.

Contents

1. Introduction

Threshold fjords are fjords where the mouth is partially cut off from the sea by a sill that is more shallow than the inner part of the fjord. The sill acts as a barrier for the inflowing coastal water (Sverdrup, Johnson, Fleming, et al., 1942; Aure & Stigebrandt, 1989). The water masses in the inner part of the fjord, below the sill depth, will in this thesis be termed basin water. In threshold fjords, basin water is known to evolve into a hypoxic or even anoxic state due to a weak ventilation (Sverdrup et al., 1942). In some threshold fjords, the deepest portion of the basin water may have a residence time of several years, causing oxygen depletion (Soltveit & Jensen, 2017).

Globally, there has been a decline in the total amount of dissolved oxygen in the oceans (Schmidtko, Stramma, & Visbeck, 2017; Breitburg et al., 2018). This can pose a potentially larger treat to the ecological conditions in the specific environment of a threshold fjord. Previously it has been shown that a greater amount of the basin water in several threshold fjords experiences oxygen depletion (Soltveit & Jensen, 2017; Breitburg et al., 2018). A proposed solution to this problem could be to increase the circulation and/or ventilation of the basin water.

The basin water can be exchanged naturally by both advective and diffusive processes (Aure & Stigebrandt, 1989), where the diffusive process is the vertical diffusion in the basin area. According to Liungman and Rydberg (2001) there are two key advective processes regarding renewal of the basin water. Firstly, the exchange across the sill, and secondly, descent and intrusion of the inflowing denser water, also called high-density intrusion (Aksnes, Aure, Johansen, Johnsen, & Salvanes, n.d.). The natural forces that can influence these advective processes are the tide and the wind stress, but sometimes they are not strong enough to make a full or even a partial renewal of the basin water (Liseth, 1977; Liungman et al., 2001; Aure & Stigebrandt, 1989). The density of the outer water is of importance, since the water at sill level must be denser than the basin water to replace it. If a high-density intrusion occurs, it usually benefits the ecological conditions due to a higher concentration of dissolved oxygen in the intruding coastal water (Aure & Stigebrandt, 1989).

When the advective processes are incapable of exchanging the basin water and the vertical diffusion is the only process that contributes to the exchange, we have a stagnation

period (Aure & Stigebrandt, 1989). In such cases, the concentration of dissolved oxygen in the basin will decrease (Aksnes et al., n.d.). Vertical diffusion of oxygen in deeper basins is minor compared to the biological consumption, and the decay rate of oxygen is therefore approximately equal to the biological consumption (Aure & Stigebrandt, 1989; Aksnes et al., n.d.). The deepest portion of the basin water will in time evolve towards an anoxic state. In some Norwegian fjords this is becoming reality (Soltveit & Jensen, 2017; Aarre, Andersson, Lambrechts, & Eriksen, 2016). These fjords have many fish farms, which results in nutritious organic matter sinking down towards the bottom. Bacteria that resides in the depths decomposes this organic matter and uses oxygen in the process. This bacterial metabolism can in cases of reduced oxygen supply result in the generation of hydrogen sulphide, which can cause fatal living conditions for other species (Sverdrup et al., 1942). The main reason for the poor ecological conditions in the depths is a lack of high-denisity intrusion, however the fish farms may contribute to worsen the problem (Soltveit & Jensen, 2017).

Upwelling is a phenomenon where nutritious water from the depths flows towards the photic zone near the surface. This results in high primary production and occurs naturally along the coast of Peru, for instance (Trujillo & Thurman, 2017).

Inspired by this, attempts to create artificial upwelling has been conducted to enhance the primary production. The main methods to induce artificial upwelling are submerged fresh (or brackish) water discharge or a so-called bubble curtain, and this has been attempted in simulated numerical models and real-life projects (Aure, Strand, Erga, & Strohmeier, 2007; Maruyama, Tsubaki, Taira, & Sakai, 2004; Berntsen, Aksnes, & Foldvik, 2002; McClimans, Handå, Fredheim, Lien, & Reitan, 2010; Strand et al., 2014). In this study, the same principle will be used to investigate if a submerged fresh water discharge, placed at the bottom of a threshold fjord, can increase the circulation and/or ventilation of the basin water.

A discharge of one fluid into another fluid can be defined as a jet, a plume or a buoyant jet, where the first indicates a purely momentum driven process, the second a purely buoyancy driven process and the third a combination of the two (Fischer, List, Koh, Imberger, & Brooks, 1979). In this study, as fresh water is discharged into denser water with relatively small velocities, the process is mostly buoyancy driven, resulting in a plume. This also can be referred to as a buoyant plume to specify the driving force (Fischer et al., 1979; Turner, 1969).

Sørfjorden is a fjord located east of Bergen, Norway, at approximately 60.4°N and 5.5°E.

It is a threshold fjord with problematic conditions regarding the levels of dissolved oxygen, especially in the basin depths (Johansen et al., 2018). Since it may seem as the natural processes regarding water renewal are insufficient, the fjord could possibly benefit from artificial upwelling.

Sørfjorden will be used as the model fjord for this study. Numerical experiments will be performed to explore possibilities of exchanging the basin water by creating artificial upwelling. A map of the fjord and its geographic area is shown in Fig. 1.1. The colours in the figure gives an indication on the depth of the fjord; darker blue is deeper and lighter is more shallow.

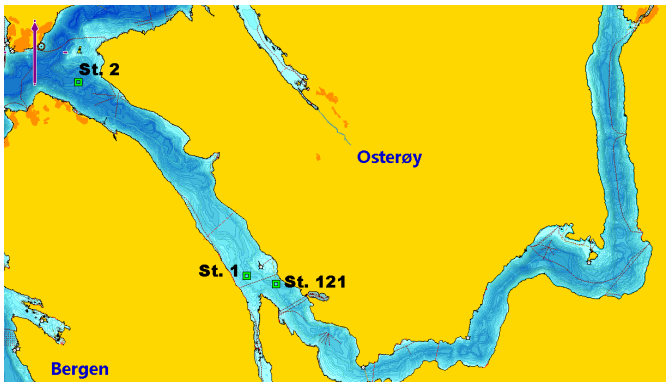

Fig. 1.1. Map showing Sørfjorden and the stations data was collected from. [Courtesy of Einar Bye-Ingebrigtsen, UniResearch, pers. comm.]

For the numerical experiments to have a realistic foundation, data measured in Sørfjorden will be used for the variables such as salinity, temperature and concentration of dissolved oxygen. In Fig. 1.1 the labels St. 1, St. 2 and St. 121 indicates the stations of measurement for these data. Section 3.3 describes in more detail how these data are used. St. 2 is placed in the entrance region of the fjord, St. 1 and St. 121 are placed in a more shallow area, i.e. at the sill.

The aim of this thesis is to study effects of submerged fresh water as an attempt to increase the ventilation and/or circulation of a threshold fjord.

Chapter 2 presents the numerical model used in this study. It describes the assumptions the model is built upon and briefly explains some of the numerical techniques of this ocean model. It presents the equations that the model is built upon, and defines the variables in the equations.

Chapter 3 specifies the model set-ups for this study. It also describes how initial and

boundary values for the different variables are chosen. Methods of measurement used for the analysis are also presented.

Chapter 4 presents and discusses results from the preliminary experiments, and is followed by Chapters 5 to 8, which presents each of the four main experiments performed. Results are presented and discussed, and natural comparisons are done consecutively.

In Chapter 9 the main findings of the experiments are summed up and discussed. A conclusion is proposed, as well as suggestions for further work.

2. The numerical model

2.1 The Bergen Ocean Model

The numerical model used in this study is the Bergen Ocean Model (BOM). It is a three-dimensional *σ-coordinate mode-split* model. These terms will be briefly explained.

The equations described in the following section, are transformed into a terrain-following[1] σ-coordinate system according to Blumberg & Mellor (1987). Advantages of using the σ-coordinate system is that the bottom and free surface always will be a coordinate surface, and the horizontal layers follows the topography of the model domain (Phillips, 1957).

The CFL (Courant-Friedrichs-Lewy) criterion gives a restriction on the time step for a given grid size and advective velocity. For the fastest modes, shorter time steps are required. For the computational economy it is desired to have time steps as long as possible. Instead of being limited to use the shorter time steps given by the CFL criterion for all computations, mode-splitting, as described in (Blumberg & Mellor, 1987; Berntsen, 2004) is applied.

2.2 Governing equations

In this section the variables and their governing equations used in this model will be presented. The variables are specified by a location given by the Cartesian three-dimensional coordinates, x, y, z, and a time, t. By describing the equations in Cartesian coordinates it indicates that the curvature effects of the earth are neglected due to a relatively small domain. The equations are written in vector-notation, but in the model they are discretized on an Arakawa C-grid, which is a staggered grid with many numerical advantages (Haltiner & Williams, 1980). See (Mesinger & Arakawa, 1976) or (Berntsen, 2004) for further description of the C-grid.

The continuity equation for an incompressible fluid (conservation of volume) is

$$\nabla \cdot \vec{U} + \frac{\partial W}{\partial z} = 0, \tag{2.1}$$

[1] Fig. 3.2 in Chapter 3 will show an example of this.

where ∇ is the operator $(\frac{\partial}{\partial x}, \frac{\partial}{\partial y})$. Since the horizontal and vertical scales tends to be different in geophysical modelling, they are often separated in the equations. Therefore $\vec{U} = (U, V)$ is the horizontal velocity vector with U the velocity component in the x-direction and V the velocity component in the y-direction and W is the velocity component in the z-direction.

The momentum equations for turbulent flow, after Reynolds time averaging (Berntsen, 2004), are

$$\frac{\partial U}{\partial t} + \vec{U} \cdot \nabla U + W\frac{\partial U}{\partial z} - fV = -\frac{1}{\rho_0}\frac{\partial P}{\partial x} + \frac{\partial}{\partial z}\left(K_M \frac{\partial U}{\partial z}\right) + F_x, \tag{2.2}$$

$$\frac{\partial V}{\partial t} + \vec{U} \cdot \nabla V + W\frac{\partial V}{\partial z} + fU = -\frac{1}{\rho_0}\frac{\partial P}{\partial y} + \frac{\partial}{\partial z}\left(K_M \frac{\partial V}{\partial z}\right) + F_y, \tag{2.3}$$

$$\rho g = -\frac{\partial P}{\partial z}, \tag{2.4}$$

where f is the Coriolis parameter, ρ is the density, g is the gravitational acceleration and P is the pressure. In this study the Coriolis parameter is set equal to zero. With the Boussinesq approximation, the changes in density are neglected except in the gravity term, therefore ρ_0 is a constant reference value (Haidvogel & Beckmann, 1999). The momentum diffusion, also called the viscosity, is split into a vertical and a horizontal component, where K_M is the vertical component. The horizontal viscosity terms are F_x and F_y. In section 2.4 the viscosity terms will be further discussed.

The momentum equation in the vertical direction can, when the horizontal scale is much larger than the vertical scale, be simplified assuming that the gravitational forces balances the vertical pressure gradient (Haidvogel & Beckmann, 1999), as seen in equation (2.4). This is referred to as the hydrostatic approximation. This assumption indicates that the other terms in the vertical momentum equation are of negligible size, i.e. unlikely to be important (Haidvogel & Beckmann, 1999). By integrating equation (2.4) vertically the pressure at depth z can be obtained by

$$P(x, y, z, t) = g\rho_0\eta(x, y, t) + g\int_z^0 \rho(x, y, Z)dZ, \tag{2.5}$$

where $\eta = \eta(x, y, t)$ is the surface elevation, which is evaluated by the depth integrated continuity equation as described in (Blumberg & Mellor, 1987).

The equation governing the transport of salinity, S, and temperature, T, are of the form

$$\frac{\partial \theta}{\partial t} + \vec{U} \cdot \nabla \theta + W \frac{\partial \theta}{\partial z} = \frac{\partial}{\partial z} \left(K_H \frac{\partial \theta}{\partial z} \right) + F_\theta, \tag{2.6}$$

where θ represents either S or T. The effects of diffusivity is represented by a vertical and a horizontal component, where K_H is the vertical component. The horizontal diffusion term is F_θ. The diffusive terms will be further discussed in section 2.4.

The density is computed according to an equation of state of the form

$$\rho = \rho\left(T, S\right), \tag{2.7}$$

which in this study is the equation given in Wang (1984).

2.3 Boundary conditions

The top of the ocean is a free surface, and we have

$$\rho_0 K_M \left(\frac{\partial U}{\partial z}, \frac{\partial V}{\partial z} \right) = \left(\tau_{0x}, \tau_{0y} \right), \tag{2.8}$$

$$\rho_0 K_H \left(\frac{\partial T}{\partial z}, \frac{\partial S}{\partial z} \right) = \left(\dot{T}_0, \dot{S}_0 \right), \tag{2.9}$$

where (τ_{0x}, τ_{0y}) is the wind stress and $(\dot{T}_0, \dot{S}_0)$ the net heat flux and the net evaporation at the surface, respectively. In this study, these are equal to zero.

The vertical velocities at the free surface and at the bottom are given by

$$W_s = U_s \frac{\partial \eta}{\partial x} + V_s \frac{\partial \eta}{\partial y} + \frac{\partial \eta}{\partial t}, \tag{2.10}$$

$$W_b = -U_b \frac{\partial H}{\partial x} - V_b \frac{\partial H}{\partial y}, \tag{2.11}$$

where the notations of 'underline s' and 'underline b' indicates the values near the surface and bottom, respectively. The surface velocity of W is given by the varying sea elevation, and at the bottom the flow is parallel to the slope.

The bottom drag affects the horizontal velocities by

$$\rho_0 K_M \left(\frac{\partial U}{\partial z}, \frac{\partial V}{\partial z} \right) = (\tau_{bx}, \tau_{by}), \tag{2.12}$$

where (τ_{bx}, τ_{by}) is the bottom drag stress, which is specified by a quadratic drag law

$$\vec{\tau_b} = \rho_0 C_D |\vec{U}_b| \vec{U}_b, \tag{2.13}$$

where the drag coefficient C_D is given by

$$C_D = \max \left[0.0025, \frac{\kappa^2}{(ln(z_b/z_0))^2} \right]. \tag{2.14}$$

Here, z_b is the distance from the nearest grid point to the bottom, and z_0, the bottom roughness parameter, is 0.001 m. The von Karman constant, κ, is 0.4.

2.4 Turbulence closure

In the preceding sections, the governing equations for the independent variables are given. In most cases the viscosity and diffusivity coefficients can not be set constant, but must be evaluated through special equations or turbulence models in order to close the system. Mathematically, it is the non-linear, advective term in the momentum conservation equations (2.2) and (2.3) that makes the prediction of turbulence difficult.

Since the model area has to be discretized into grid cells, some motion will occur at sub-grid scale and then be unresolved (Cushman-Roisin & Beckers, 2011). These unresolved motions affects the larger resolved motions, and must be taken into account; they are parametrized by eddy viscosity and diffusivity terms (Cushman-Roisin & Beckers, 2011). Since the vertical grid size is smaller than the horizontal, it will cover a smaller amount of the unresolved motions. Two parameters are therefore needed to parametrize the dissipative subgrid effect of turbulence: a vertical and a horizontal eddy viscosity, K_M and A_M, where K_M is smaller than A_M (Cushman-Roisin & Beckers, 2011). To account for the subgrid mixing effect from turbulence, the molecular diffusion of heat and salt are replaced by vertical and horizontal *eddy* diffusivity, K_H and A_H (Cushman-Roisin & Beckers, 2011).

2.4.1 Horizontal closure

In equation (2.2) and (2.3) the terms F_x and F_y are given by

$$F_{x,y} = \frac{\partial}{\partial x} \left(A_M \frac{\partial (U,V)}{\partial x} \right) + \frac{\partial}{\partial y} \left(A_M \frac{\partial (U,V)}{\partial y} \right). \tag{2.15}$$

In equation (2.6) the term F_θ, with θ as S or T, is given by

$$F_\theta = \frac{\partial}{\partial x}\left(A_H \frac{\partial \theta}{\partial x}\right) + \frac{\partial}{\partial y}\left(A_H \frac{\partial \theta}{\partial y}\right). \tag{2.16}$$

The horizontal viscosity and diffusivity coefficients, A_M and A_H, may be computed according to Smagorinsky (1963), or chosen to be constant in space and time. In this study constant values were set, they will be specified later. It could be noted that while these in theory are meant to parametrize subgrid scale processes, they are in practice often used to dampen small-scale computational noise (Blumberg & Mellor, 1987).

2.4.2 Vertical closure: The Mellor and Yamada 2.5 level model

Without equations for the vertical eddy viscosity/diffusivity, K_M/K_H, the system is not closed. The easiest way is to set them constant, but in most cases it is not sufficient, since they are dependent on the stratification and the shear forces in the fluid, which will vary in time and space.

In some cases they can be evaluated by a simple model, but in cases where both stratification and tidal forcing are of importance, the Mellor and Yamada Level 2.5 turbulence model can be suitable (Berntsen, 2004). This turbulence model covers some important properties and complexity of turbulence; the vertical mixing should decrease in a strongly stratified (stable) fluid and increase by increasing shear. This turbulence model also includes the effects at the boundaries (Blumberg & Mellor, 1987; Mellor & Yamada, 1982).

The Richardson number,

$$Ri = -\frac{g}{\rho_0} \frac{\dfrac{\partial \rho}{\partial z}}{\left(\dfrac{\partial U}{\partial z} + \dfrac{\partial V}{\partial z}\right)^2}, \tag{2.17}$$

is a ratio between the vertical density gradient and the velocity shear, and works as an indicator on how turbulent the flow is. The Mellor and Yamada 2.5 level model is responsive to this ratio. In equations (2.18) and (2.19) the second term on the right side includes the shear velocities and the third term the vertical density gradient. When the shear velocities are large, more turbulence is produced. If the vertical density gradient is large (and negative) the turbulence is dampened; a large and negative density gradient stabilizes the field.

The following equations are based the turbulence model description given by Blumberg & Mellor (1987). The equations for turbulent kinetic energy, $0.5q^2$, and turbulent macro scale, l, are

$$\frac{\partial q^2}{\partial t} + \vec{U} \cdot \nabla q^2 + W\frac{\partial q^2}{\partial z} = \frac{\partial}{\partial z}\left(K_q \frac{\partial q^2}{\partial z}\right) + 2K_M\left[\left(\frac{\partial U}{\partial z}\right)^2 + \left(\frac{\partial V}{\partial z}\right)^2\right] + \frac{2g}{\rho_0}K_H\frac{\partial \rho}{\partial z} - \frac{2q^3}{B_1 l} \tag{2.18}$$

$$\frac{\partial q^2 l}{\partial t} + \vec{U} \cdot \nabla q^2 l + W\frac{\partial q^2 l}{\partial z} = \frac{\partial}{\partial z}\left(K_q \frac{\partial q^2 l}{\partial z}\right) + lE_1 K_M\left[\left(\frac{\partial U}{\partial z}\right)^2 + \left(\frac{\partial V}{\partial z}\right)^2\right] + \frac{lE_1 g}{\rho_0}K_H\frac{\partial \rho}{\partial z} - \frac{q^3}{B_1}\tilde{W}, \tag{2.19}$$

where K_q is the energy diffusion coefficient and

$$\tilde{W} = 1 + E_2\left(\frac{l}{\kappa L}\right)^2 \tag{2.20}$$

and where

$$L^{-1} = (\eta - z)^{-1} + (H + z)^{-1}. \tag{2.21}$$

Defining

$$G_H = \frac{l^2}{q^2}\frac{g}{\rho_0}\frac{\partial \rho}{\partial z} \tag{2.22}$$

the stability functions in the expressions for vertical diffusivity and viscosity becomes

$$S_H[1 - (3A_2B_2 + 18A_1A_2)G_H] = A_2[1 - 6A_1/B_1] \tag{2.23}$$

and

$$S_M[1 - 9A_1A_2G_H] - S_H[18A_1^2 + 9A_1A_2)G_H] = A_1[1 - 3C_1 - 6A_1/B_1]. \tag{2.24}$$

The empirical values in the expressions above, obtained by tank experiments, are

$$(A_1, A_2, B_1, B_2, C_1, E_1, E_2) = (0.92, 0.74, 16.6, 10.1, 0.08, 1.8, 1.33).$$

K_M, K_H and K_q are then computed according to

$$K_M = lqS_M, \tag{2.25}$$
$$K_H = lqS_H, \tag{2.26}$$
$$K_q = 0.20lq, \tag{2.27}$$

Boundary conditions for l and q^2 at the free surface are

$$q^2 = B_1^{2/3} u_{\tau s} \tag{2.28}$$
$$l = 0, \tag{2.29}$$

where $u_{\tau s} = (\vec{\tau_0}^2)^{1/2}$, with $\vec{\tau_0}$ as the surface wind stress. At the bottom

$$q^2 = B_1^{2/3} u_{\tau b}, \tag{2.30}$$
$$l = 0, \tag{2.31}$$

where $u_{\tau b} = (\vec{\tau_b}^2)^{1/2}$, with $\vec{\tau_b}$ as the bottom drag stress.

Critical Richardson number

There is a limit where the flow changes its regime from a stable to an unstable one, and turbulence dominates. The Richardson number has a critical value, Ri_C, to represent this regime shift. It is not a specific value where this regime shift happens, but the value 0.25 is often used since it is the necessary condition for instability (Kundu, Cohen, & Dowling, 2016). The Mellor-Yamada turbulence model is designed to respond to the Richardson number. When $\mathrm{Ri} \leq \mathrm{Ri}_C$ the turbulence kinetic energy, q^2, and the turbulence length scale, l, increases. The vertical mixing coefficients, K_M and K_H, then increases. The dynamics and mixing around submerged discharges are influenced by the turbulence kinetic energy and the turbulence length scale, which means that the values of the vertical mixing coefficients are of special importance with submerged discharges.

3. The model domain and set-ups

3.1 The model area and grid resolution

As mentioned, Sørfjorden will be the model area for this study. The model domain is an idealized version of Sørfjorden, with one distinct sill with depth of 200 m, and the rest of the fjord with a depth of 400 m, illustrated in Fig. 3.1. For the purpose of this study, the simplicity of the topography is assumed appropriate. The centre of the sill is approximately 10 km into the fjord from the mouth, shown in Fig. 3.1. The length of the fjord is 35.5 km and the width 2 km, which includes the boundaries/land cells, seen in Fig. 3.1. The area is discretized on a grid with $\Delta x = 250$ m and $\Delta y = 250$ m, resulting in 142 cells in the x-direction and 8 cells in the y-direction. To indicate the position of the grid cell in the horizontal directions, the indices i and j are used for the x- and y-direction, respectively.

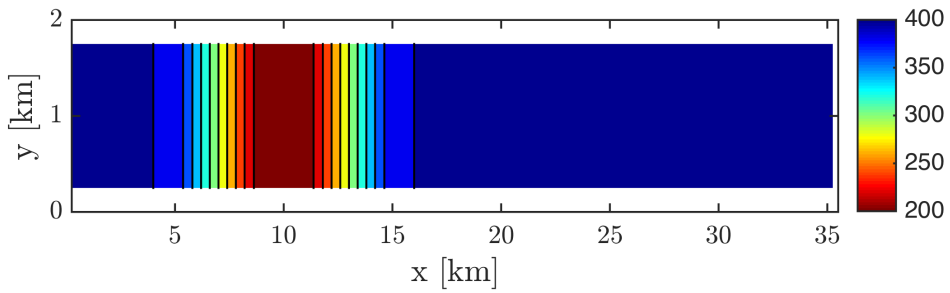

Fig. 3.1. The model of Sørfjorden seen from above. Contours of the depth is shown. The white areas in the upper, bottom and right side indicates closed boundary/land.

The resolution in the vertical direction should be high enough to resolve the vertical gradients such as the salinity and temperature fields. In areas with steep topography, like the sill in this case, the resolution is especially of importance since one grid cell can cover a large distance in the vertical direction due to the vertical stretching of the cell by σ-layers, see Fig. 3.2. To resolve the vertical scales and still attain a reasonable run time, 61 σ-layers were applied.

The bottom is defined by a bottom matrix, $H_{i,j}$, which gives the depth at the centre of each grid cell (i, j). A linear Shapiro filter (Shapiro, 1975) was used four times on the bottom matrix in the x-direction to smooth $H_{i,j}$ around the sill. The sill was originally

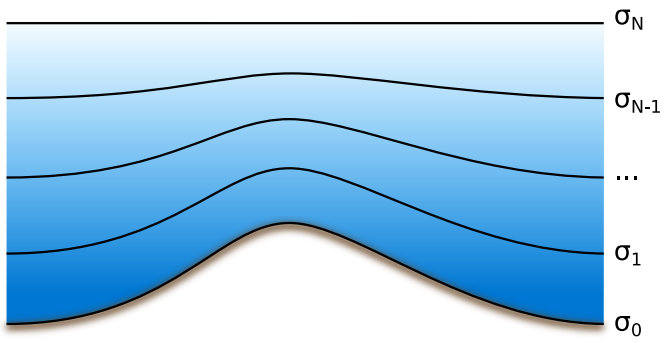

Fig. 3.2. Example of σ-layers. Source: `https://commons.wikimedia.org/wiki/File:Sigma-z-coordinates.svg#/media/File:Sigma-z-coordinates.svg`

created by linear slopes from the basin depth of 400 m to the sill depth of 200 m, giving sharp edges at the bottom. Fig. 3.3 shows the results of the smoothing. The Shapiro filtering on the bottom matrix $H_{i,j}$ one time is

$$\bar{H}_{i,j} = \frac{1}{4}(H_{i+1,j} + 2H_{i,j} + H_{i-1,j}), \tag{3.1}$$

where $\bar{H}$ is the filtered matrix.

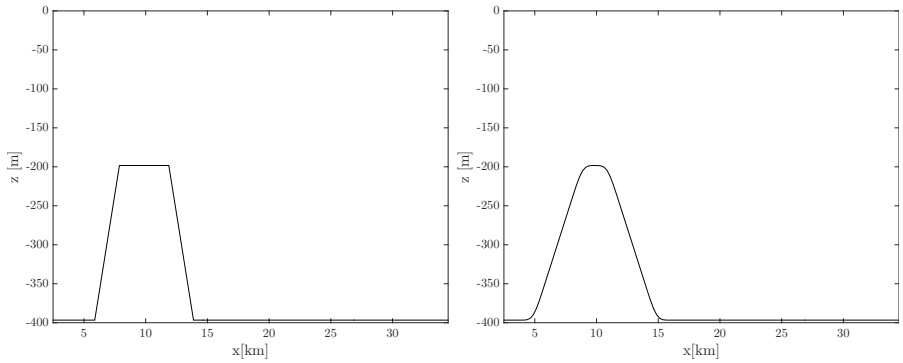

Fig. 3.3. The bottom of the fjord seen in a vertical plane before and after the Shapiro filtering. Note that the units on the x-axis are in km, and the z-axis in m. The slope steepness is approximately 0.04.

3.2 Time steps

By applying mode-split, several two-dimensional, depth integrated steps are computed for a full three-dimensional step. In this study, the three-dimensional time step is 9 s and there are 30 two-dimensional time steps per three-dimensional step.

3.3 Initial values

Initially, everything is at rest, with $U = V = W = 0$ ms^{-1} and $\eta = 0$ m. For the other field variables, the initial values were set based on data collected from Sørfjorden.

3.3.1 Salinity and temperature

The density is computed according to the equation of state from Wang (1984), $\rho = \rho(S, T)$. Initial values of the salinity and temperature are thus needed. Initial profiles for salinity and temperature were constructed from data measured at three stations[1] in Sørfjorden.[2] Since the data was collected at different times and places, they were averaged in both time and space, smoothing the seasonal changes of salinity and temperature. Using the N observations of the salinity and temperature at each depth, the profiles were computed by

$$\theta(z) = \frac{1}{N} \sum_{\forall x,y,t} \theta_{obs}(x, y, z, t), \tag{3.2}$$

where θ is either S or T and θ_{obs} is the measured salinity or temperature at a specific station at a specific depth and time.

Profiles of S and T were produced for 29 different depths. The salinity values were sorted by ascending values and the temperature values by descending values. By the equation of state and the range of S and T in this case, this results in a stably stratified initial condition, $\frac{\partial \rho}{\partial z} \geq 0$.

A linear interpolation was done to give initial values at the depths defined by the σ-layers. The linear Shapiro filter, equation (3.1), was used four times on the profiles in the vertical direction to achieve smooth profiles.

The initial values of salinity and temperature gave initial values of the density as seen in Fig. 3.4. Two figures are included, to show both how the densities from 1016-1027 kg/m^3 are distributed, and the distribution in the depths, from 1027-1027.2 kg/m^3. As the figure illustrates, the isopycnals are not straight horizontal lines above the sill, due to errors in the interpolation to a σ-grid. This is an artifact of the σ-layers.

[1] St.1, St.2 and St.121 in Fig. 1.1

[2] Courtesy of Einar Bye-Ingebrigtsen, UniResearch, pers. comm.

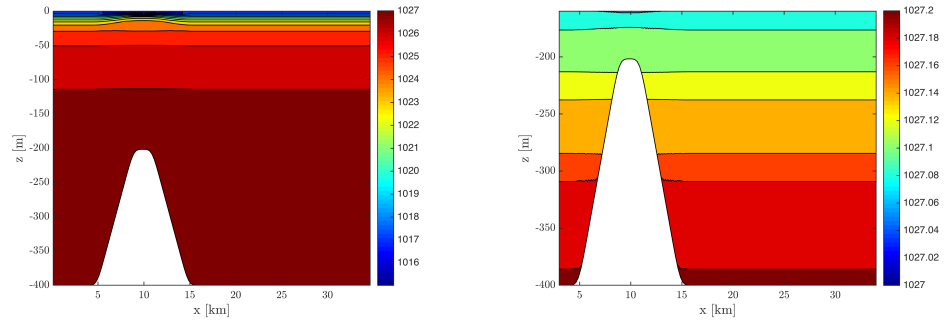

(a) The vertical profile.

(b) Below 160 m depth.

Fig. 3.4. Initial values of the density, ρ [kg/m^3], shown in the vertical plane through the y-directional centre.

3.3.2 Passive scalars

Two passive scalars are added to the model; one to model the dissolved oxygen and one as a tracer for the basin water.

Dissolved oxygen

To study the evolution of the dissolved oxygen in the fjord, it was added as a passive scalar. The initial values were based on data collected evenly through 2016 and 2017.[3] Data from two stations were analysed, one located outside the sill and one located in the area of the basin. Since the values of dissolved oxygen measured outside the sill was higher than the ones inside the basin, two profiles overlapping at the point right above the sill was made. The oxygen levels varies throughout the year due to biological processes. To even this out an averaging on the data was done, similar to the one in equation (3.2). The vertical profile of dissolved oxygen was also smoothed, using the Shapiro filter (3.1) four times. Dissolved oxygen was added to the system as a passive tracer following equation (2.6). The initial field for dissolved oxygen is shown in Fig. 3.5. Concentrations below 2 ml/L are considered as hypoxic water (Wolanski, 2015). Most of the basin water are in fact initially hypoxic.

In stagnation periods, the biological consumption will result in an oxygen decay which can be represented by a parameter, b (Aksnes et al., n.d.). An estimation on b for this model was calculated based on the same data as the oxygen profile. It may be noted that the background vertical diffusion in a stratified fjord is weak compared with the biological consumption. The value of b is estimated from stagnation periods and

[3]Courtesy of Trond Einar Isaksen, UniResearch, pers. comm.

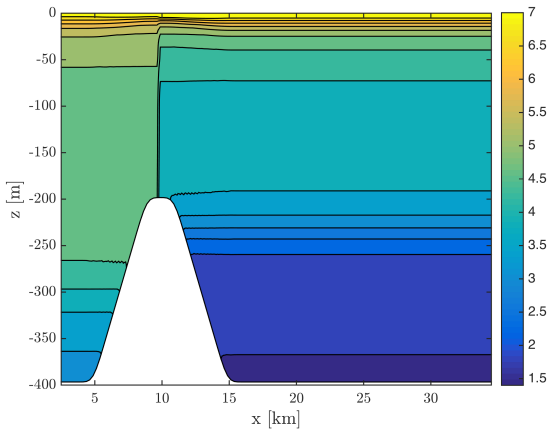

Fig. 3.5. Contour of the initial values of dissolved oxygen [ml/L] in the vertical plane through the y-directional centre. The inner and outer profiles overlaps above the sill.

therefore, in essence, reflects the biological consumption (Aksnes et al., n.d.). The values of the dissolved oxygen were plotted against time for each depth. An almost linear decay from the first to the last measure was observed in some data sets. These were the data collected inside the basin, in other words below sill depth and from the inner station. An average of these decays could then be computed according to

$$b = \frac{1}{N} \sum_{A} \frac{\Delta O_2}{\Delta T}, \quad A = \{\text{All data sets below sill depth}\} \tag{3.3}$$

where N is the number of slopes being averaged, ΔT is the time period from the first to the last measure, given in seconds, ΔO_2 is the difference between the highest/first observed and lowest/last observed value of dissolved oxygen, given in ml/L. The value of b was estimated to $1.4 \cdot 10^{-8}$ ml/L per second, or $1.2 \cdot 10^{-3}$ ml/L per day. This was added as a sink term in the governing equation for the dissolved oxygen.

Passive tracer

All the water below 300 m in the basin was initially marked using a tracer. This was done to study the evolution and the transport of the deepest portion of the basin water. The initial values for the passive tracer, γ, were

$$\gamma(x, y, z) = \begin{cases} 1, & \text{if } x > 10000 \text{ m and } z \leq -300 \text{ m} \\ 0, & \text{else.} \end{cases} \tag{3.4}$$

In Fig. 3.6 the initial values are shown. There is some noise near the sill, this is due to the σ-layers tilting the grid cells near the slope as is seen in Fig. 3.2. In flat areas the depth of a σ-layer is constant, but when facing slopes such as the sill, the depth of the σ-layer changes as it follows the terrain.

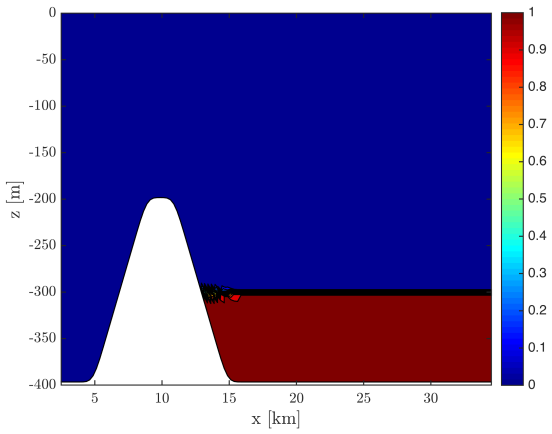

Fig. 3.6. Contour of the initial values of the passive tracer in the vertical plane through the y-directional centre. The tracer is dimensionless.

3.4 Boundary conditions

The model area has closed boundaries everywhere there is land. For this domain, the shore/land are the side walls to the east, north and south. The bottom of the fjord is also land, i.e. a closed boundary. Through these closed boundaries there is no volume flux, which means that there are no advective or diffusive heat and salt fluxes, as well as no fluxes of the passive tracers. The boundaries mentioned so far are natural boundaries which are determined by the physics involved (Røed & Cooper, 1986). At the mouth of the fjord, i.e. to the left side of the domain, the computational domain is cut off at a location where there is water and not land. This calls for an artificial boundary condition to make the fjord interact with the outside in a realistic matter (Røed & Cooper, 1986). The boundary conditions at the open boundary will be specified in the following.

3.4.1 The open boundary at the mouth of the fjord

One way of implementing an open boundary, is through a flow relaxation scheme (FRS) zone. FRS was originally designed to be used as a matching scheme when going from an external to an internal solution with different mesh sizes in meteorology, but it can

also be used as an open boundary condition (Martinsen & Engedahl, 1987). The FRS zone is in this case the area from the open boundary and ten grid cells into the fjord. At each time step in the model, the FRS updates each prognostic variable, ϕ, according to

$$\phi = (1 - \alpha)\phi_M + \alpha\phi_F, \tag{3.5}$$

where ϕ_M represents the values computed by the model and ϕ_F the forced solution in the FRS zone (Martinsen & Engedahl, 1987). The relaxation parameter α varies from 1 at the boundary to 0 at the end of the FRS zone.

In this study, the variables S, T and O_2 are relaxed towards a forced solution at the boundary through the FRS zone. The outer values of these variables are assumed equal to the initial conditions. However, it was important that the fresh water from the outlets were let out. A condition similar to the one in Berntsen et al. (2002) was put on the forced solution, ϕ_F, where ϕ is either S, T or O_2.

$$\phi_F = \begin{cases} \phi_0, & \text{if} \quad \overline{U} \geq 0 \\ \overline{\phi_M}, & \text{if} \quad \overline{U} < 0, \end{cases} \tag{3.6}$$

where $\overline{U}$ and $\overline{\phi_M}$ indicates an average value of the variable over the ten grid cells next to the FRS zone and ϕ_0 indicates the initial value of the variable. For inflow, the coastal water enters the fjord. For outflow, the interior water are allowed to exit the fjord.

The passive tracer, γ, was set equal to zero in the forced solution. The velocity component in the y-direction was relaxed towards zero through the FRS zone. For the velocity component in the x-direction, a Neumann condition was applied, with the gradient equal to zero. This was done to conserve the volume when sources of fresh water was added to the system.

Tidal constituents

The tidal was imposed as a boundary condition for the sea elevation. Four constituents of the tide were included, each defined by a sinusoidal function for the varying sea elevation. The constituents are given in Table 3.1, and the notations M_2, S_2, N_2 and K_2 are as described in (Kantha & Clayson, 2000). These mimic the semi-diurnal tide that is most dominant in the coastal area of the Atlantic (Kantha & Clayson, 2000).

Component	Period [hr]	Amplitude [m]	Phase offset
M_2	12.42	0.45	312°
S_2	12.00	0.16	353°
N_2	12.66	0.09	290°
K_2	11.97	0.05	351°

Table 3.1. The tidal constituents used in the study.

3.5 Measuring effects of fresh water discharge

The goal of this study is to investigate effects of submerged fresh water and examine if it can benefit the ventilation and/or circulation of the threshold fjord. Some measurements to be used in this investigation is presented in the following.

The water below 300 m in the basin was marked by a passive tracer as described in equation (3.4). The volume of this marked water remaining below 300 m is computed by

$$V_\gamma(t) = \int_{10\text{ km}}^{35.5\text{ km}} \int_{0}^{2\text{ km}} \int_{-H}^{-300\text{ m}} \gamma(x, y, z, t)\, dxdydz. \tag{3.7}$$

The decay of V_γ is assumed to be exponential,

$$V_\gamma(t) = V_0 e^{-\lambda t}, \tag{3.8}$$

where λ is the decay constant, V_0 is the initial volume of the marked water and $V_\gamma(t)$ is the remaining volume of this marked water in the basin as a function of time, t.

A time scale of the reduction of V_γ is desired, as it can be used to give an indication on the residence time of the deepest portion of the basin water. It is also a good tool for comparing results from the experiments. In exponential decay models, the time it takes for the modelled quantity to be reduced to its half is defined as the half-life. The half-life, $T_{\frac{1}{2}}$, is then defined by

$$\begin{aligned} T_{\frac{1}{2}} &= -\frac{1}{\lambda} \ln\left(\frac{\frac{1}{2}V_0}{V_0}\right) \\ &= \frac{\ln 2}{\lambda}. \end{aligned} \tag{3.9}$$

The evolution of the concentration of dissolved oxygen can also be quantified by calcu-

lating how the concentration of dissolved oxygen changes in time. The integrals

$$O_{2A}(t) = \frac{1}{V_A} \int_{10\text{ km}}^{35.5\text{ km}} \int_{0}^{2\text{ km}} \int_{-100}^{0\text{ m}} O_2(x, y, z, t)\, dxdydz \tag{3.10}$$

and

$$O_{2B}(t) = \frac{1}{V_B} \int_{10\text{ km}}^{35.5\text{ km}} \int_{0}^{2\text{ km}} \int_{-H}^{-300\text{ m}} O_2(x, y, z, t)\, dxdydz \tag{3.11}$$

are used to compute the average concentration of the dissolved oxygen, as a function of time, between 0 m and 100 m depth and between 300 m and bottom depth, in the areas of the fjord past the sill. The volumes, V_A and V_B, which the integrals are divided by, are the respective volumes which the integrations are done over. The dissolved oxygen at each point and time in the domain is given by $O_2(x, y, z, t)$.

These two measures were chosen to observe the evolution of oxygen in two important regions; in the basin part and in the upper part of the fjord. It is wanted to increase the amount/concentration of dissolved oxygen in the depths, but it is just as important that the hypoxic water is transported and diluted out into the sea, and not up to the top of the fjord - suffocating the habitants there.

As a qualitative method some of the output data will be plotted to compare the differences between the results from the experiments in a visual sense.

3.6 Horizontal and vertical mixing coefficients

In the Mellor-Yamada closure model, the vertical mixing coefficients are the sum of the turbulent contribution and a constant background mixing due to for instance internal waves (Durski, Glenn, & Haidvogel, 2004; Blumberg & Mellor, 1987). This background mixing is specified by a minimum values of the vertical mixing coefficients. These are set to $2 \cdot 10^{-5}$ m^2s^{-1} because it is a usual value for the background mixing always present (Blumberg & Mellor, 1987; Berntsen, 2004).

For the horizontal mixing coefficients, A_M was set to 400 m^2s^{-1} and A_H was set to zero, except near the river outlet where A_H was set to 80 m^2s^{-1}. This was done to reduce sharp density fronts and numerical artifacts, such as undershoot, near the river outlet.

3.7 Overview of the experiments

In the next chapters, results from the numerical experiments will be presented and discussed. First, three preliminary experiments were executed, presented in Table 3.2. These were performed by adding one external force at a time, first no external forcing, then tidal forcing and finally river runoff. With these set-ups implemented, four experiments where fresh water was discharged at the bottom of the basin, followed. These are presented in Table 3.3. All of these experiments had tide and river runoff as in the third preliminary experiment. The variables of these experiments were the flux of the discharge, as well as the area of the outlet (number of bottom cells with discharge).

Prelim. experiment	Tide	River flux [m^3s^{-1}]
1	Off	0
2	On	0
3	On	10

Table 3.2. Overview of the preliminary experiments.

Exp.	Discharge flux [m^3s^{-1}]	Discharge area
1	1	$4\Delta x\Delta y$
2	10	$4\Delta x\Delta y$
3	1	$\Delta x\Delta y$
4	2	$\Delta x\Delta y$

Table 3.3. Overview of the main experiments. The discharge area is given by the grid size in the x- and y-direction, Δx and Δy.

4. Preliminary experiments

This chapter presents the results from the three preliminary experiments, one with no forcing, one with tidal forcing and one with both tidal forcing and river runoff. For these experiments, the results will be briefly presented and discussed. The focus of this study will be put on the main experiments.

4.1 No forcing

An experiment with no external forcing, also excluding the tidal, was executed as the first of the preliminary experiments.

4.1.1 First choice of simulation time

The numerical model ran for about 29 days of simulated time. The amount of the marked bottom water below 300 m did decrease some, see Fig. 4.1. In the first few days the decay might be unrealistically high due to the start-up transient. Even though the initial values for salinity and temperature gives a stably stratified density field, the discretization to the σ-layers gives some initial instabilities (Mellor, Ezer, & Oey, 1994). These instabilities are illustrated in Fig. 4.2, where the vertical and horizontal velocity field after 7.5 minutes of simulated time is shown. There is a wave pattern around the sill, which dampens out in time. These initial instabilities may enhance the mixing of the basin water and could be an answer to the higher decay seen in the first few days in Fig. 4.1.

The decay constant, $\lambda = 8.7 \cdot 10^{-4}$ day^{-1}, was computed based on the values at day 10 and day 29, omitting the first days from the calculation due to start-up transient. The half-life of the basin water, computed according to equation (3.9), is then 2.2 years.

Fig. 4.3 shows the concentration fields of the dissolved oxygen and the tracer after 29 days. Compared to the initial conditions, not much has changed. The most visible difference is that there has been some mixing of the tracer in the vertical direction. The concentration field of dissolved oxygen is similar to its initial condition, but the concentrations has, seemingly, been a little reduced. This is most visible in the basin, where the areas of the lowest concentrations has increased from the bottom 25 m of the

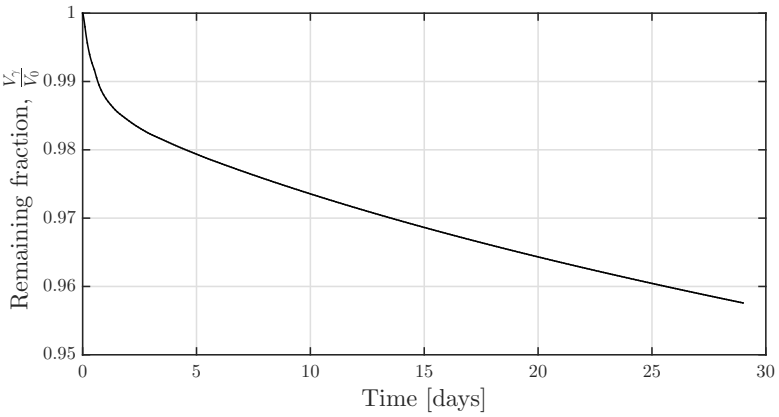

Fig. 4.1. The remaining fraction of marked bottom water below 300 m relative to its initial value, $\frac{V_\gamma}{V_0}$, plotted against time.

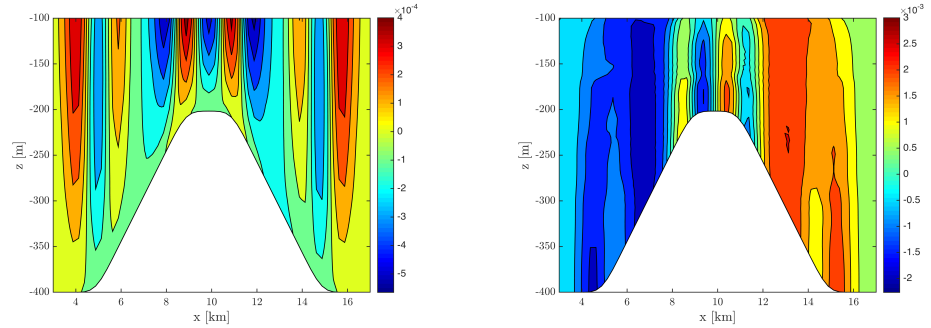

(a) W [ms^{-1}] (b) U [ms^{-1}]

Fig. 4.2. Distributions of the vertical and horizontal velocity components after 7.5 minutes, seen in the vertical plane through the y-directional centre. The visualised domain is restricted to the area near the sill.

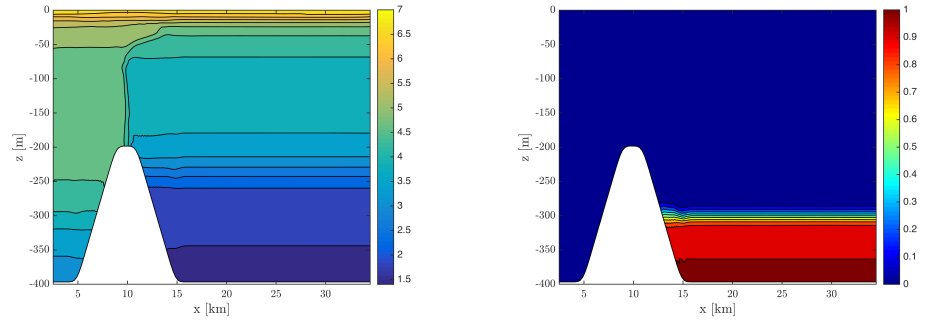

(a) (b)

Fig. 4.3. Contour of (a) the dissolved oxygen [ml/L] and (b) the passive tracer after 29 days of simulated time. The plane is a cross section through the y-directional centre.

basin initially, to the bottom 50 m of the basin at this time. This is most likely caused by the sink term representing the biological consumption.

4.1.2 A longer simulation time

A longer run, 175 days, was performed. This was done to examine if the decay constant first estimated was valid for a longer period. The decay of the marked bottom water below 300 m is shown in Fig. 4.4. Based on values of V_γ at day 10 and day 170, the decay constant was estimated to $\lambda = 5.0 \cdot 10^{-4}$ day^{-1}. This indicates a half life of 3.8 years, almost the double of the first estimation.

Fig. 4.5 shows the average concentration of dissolved oxygen in the top 100 m (dashed line) and bottom 100 m (solid line), on the inside of the sill. In both areas, the average concentration decreases. This is most likely a result of the biological consumption included in the model.

In Fig. 4.6, the concentration fields of the dissolved oxygen and tracer is shown. The tracer has spread more in the vertical direction than after 29 days, and small concentrations are visible near 250 m depth in the basin. However, most of the tracer still resides below 300 m. In Fig. 4.6a, above the sill, the shape of the contour line has changed. In the initial conditions, the outer and inner profile for the dissolved oxygen intersect above the centre of the sill. Since the values are higher outside the sill than inside, this creates a vertical contour line. This was still seen as a vertical isopleth above the sill in Fig. 4.3a, but has now almost an S-shape. It seems as though horizontal advection of the dissolved oxygen has occurred, mixing together the two profiles at the interface. This implies that there are horizontal velocities after the initial disturbances has died out, even though no external forcing is applied to the model.

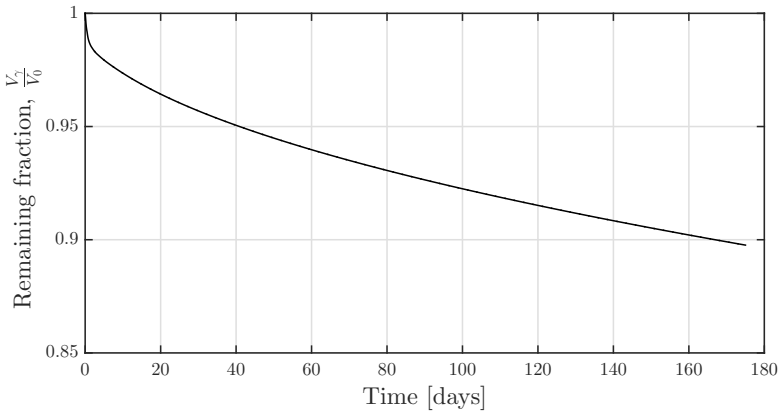

Fig. 4.4. The remaining fraction of marked bottom water below 300 m relative to its initial value, $\frac{V_\gamma}{V_0}$, plotted against time.

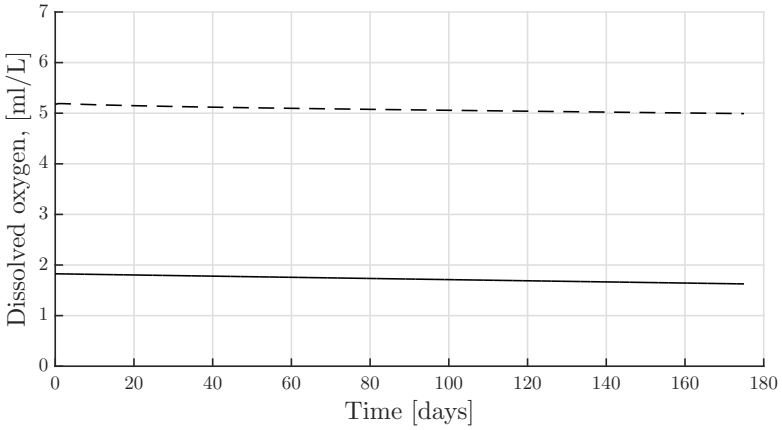

Fig. 4.5. The evolution of the average oxygen concentration below 300 m depth (solid line) and above 100 m depth (dashed line).

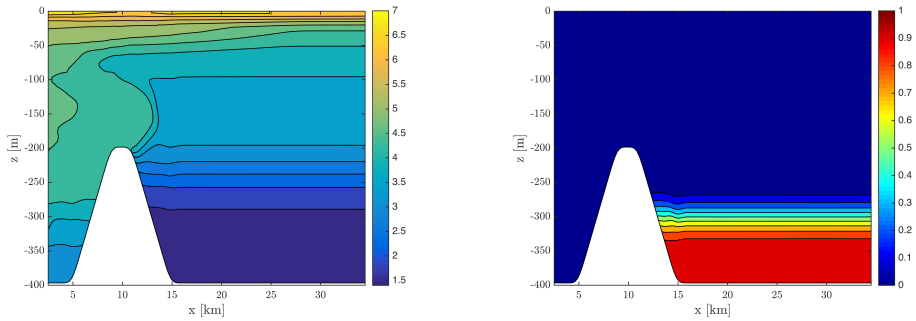

Fig. 4.6. Contour of (a) the dissolved oxygen [ml/L] and (b) the passive tracer after 175 days of simulated time. The plane is a cross section through the y-directional centre.

4.2 Tidal forcing

In the second preliminary experiment, the tidal was appended as an external force. Besides that, the experiment was identical to the first one.

4.2.1 First choice of simulation time

The decay of the marked basin water, V_γ, for a simulation time of 29 days is shown in Fig. 4.7. In the figure, there is both a red and a black curve. The red curve is the plot of the data from the simulation and the black curve is the plot of the same data smoothed. When plotting results from other experiments, only the smoothed data will be shown. The red oscillating curve has the same period as the tidal force, so it is visible that the marked bottom water is lifted up and down with the tidal. The varying amplitude is expected from the tidal constituents appended, as they are mimicking neap and spring tide (Kantha & Clayson, 2000). The smoothed data was used to estimate the decay constant, which gave $\lambda = 8.5 \cdot 10^{-4}$ day^{-1}, based on the values at day 10 and 29. This gives a half-life of 2.3 years.

The half-life of the basin water is slightly longer with the tidal than without. This might be due to the fact that with the tidal there are both diffusive and advective processes, where the advection caused by the tidal changes its direction between going into the fjord and out of the fjord. This can affect the basin water since the horizontal advective process can block the vertical transport. In the first preliminary experiment, without the tidal, there are mainly diffusive processes.

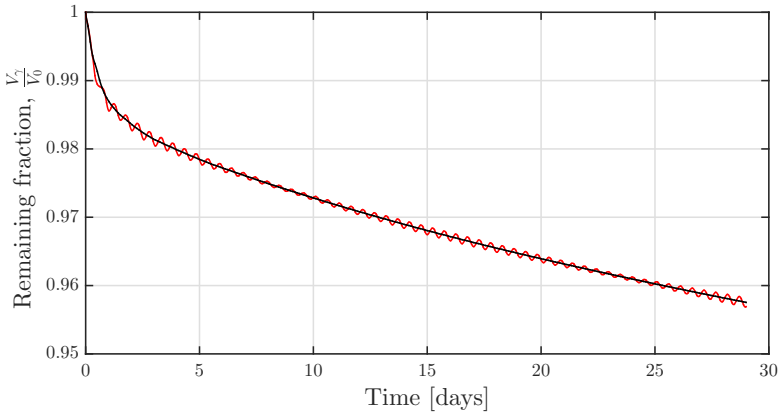

Fig. 4.7. The evolution of the amount of marked bottom water below 300 m, V_γ. The red curve shows the oscillations produced by the tidal force. The black curve is the red curve smoothed.

In Fig. 4.8, the concentration fields of the dissolved oxygen and the tracer is shown.

They compare well to the plots from the previous experiment, but some minor differences are visible. The contour lines are curved near the sill - this was not visible in the results from the previous experiment. The motion caused by the tide creates disturbances near the sill, which probably results in the curved contour lines.

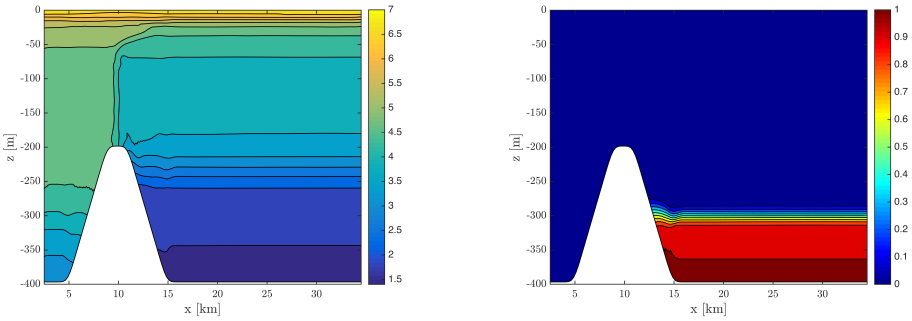

(a) (b)

Fig. 4.8. Contour of (a) the dissolved oxygen [ml/L] and (b) the passive tracer after 29 days of simulated time. The plane is a cross section through the y-directional centre.

4.2.2 A longer simulation time

A longer run was also performed for this experiment. The decay of V_γ for the longer run is shown in Fig. 4.9. Based on day 10 and 170 in this run, the decay constant was estimated to $\lambda = 4.7 \cdot 10^{-4}$ day^{-1}. This rate indicates a half-life of 4.0 years. This is of the same scale as the half-life estimated by the longer run for the previous experiment.

Fig. 4.10 shows the average concentration of the dissolved oxygen in the top 100 m (dashed line) and bottom 100 m (solid line) beyond the sill. These results compare well to the ones from the first preliminary experiment. This implies that the tide alone does not affect these concentrations much.

In Fig. 4.11a, the concentration field of the dissolved oxygen, a similar pattern as the one in Fig. 4.6a, the S-shape, is seen above the sill.

The tracer has not been transported much, but it has been diffused some more in the vertical direction, see Fig. 4.11b. The curved contour lines near the sill are also visible in these figures.

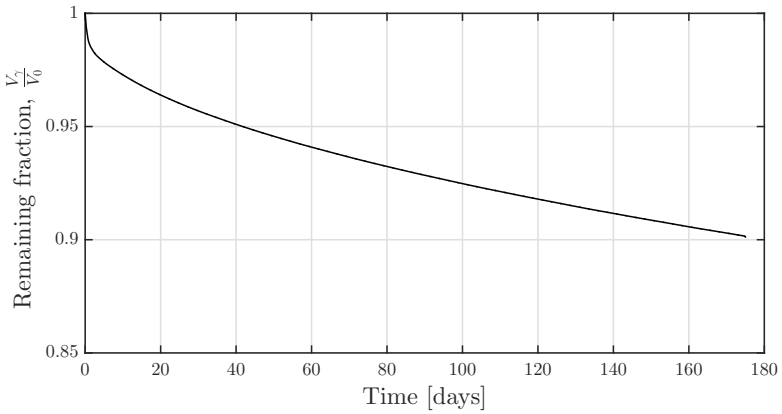

Fig. 4.9. The remaining fraction of marked bottom water below 300 m relative to its initial value, $\frac{V_\gamma}{V_0}$, plotted against time.

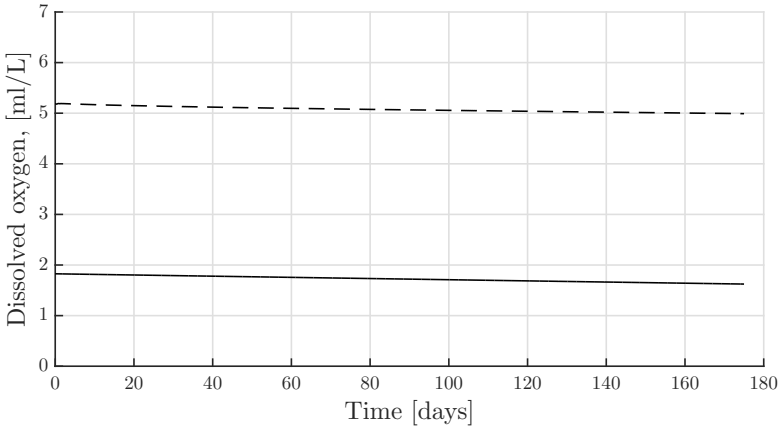

Fig. 4.10. The average oxygen concentration below 300 m depth (solid line) and above 100 m depth (dashed line), plotted against time.

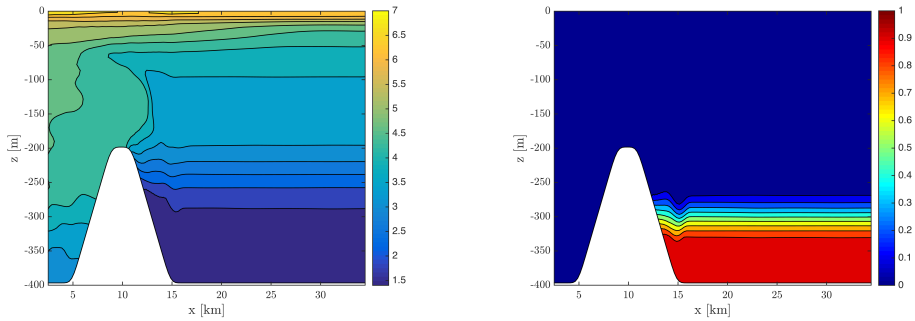

(a) Dissolved oxygen.

(b) Passive tracer.

Fig. 4.11. Contour of the passive tracer and oxygen after 175 days of simulated time. The plane is a cross section through the y-directional centre.

4.3 Tidal forcing and river runoff

The third of the preliminary experiments was executed with both tidal and river runoff as external forces. In Table 4.1, the set-ups of the river runoff is shown. The flux may be too high for dry periods, but is representative for the total flux of the rivers naturally exiting in Sørfjorden. Seasonal variations are thus neglected for this study.

Salinity, temperature and dissolved oxygen were given typical values for the rivers surrounding Sørfjorden. In the numerical model, the river runoff was located in the upper grid cells to the east. The river runoff was spread over the six internal cells at the eastern boundary, i.e. the grid cells that are not land cells, with the flux from each cell summing up to the total flux.

Total flux	**Salinity**	**Temperature**	**Dissolved oxygen**
10 m^3s^{-1}	0 psu	8 °C	7.5 ml/L

Table 4.1. Setups of the river runoff. Salinity is measured in practical salinity unit, psu.

The river runoff adds two physical factors to the model. It gives an outward current in the top layer of the fjord and enhances the stratification of the fjord by adding fresh water in the top layer. None of these are assumed to improve on the half-life of the basin water. The outward current gives some motion to the system, but is not strong enough to affect the flow in the depths. The enhanced stratification will act stabilizing to the system, and can make it more difficult for the basin water to exit the basin.

The evolution of the marked bottom water below 300 m is shown in Fig. 4.12. Around day 3, the slope is slightly reduced. It might be that the start-up transient caused by the river creates more instabilities than without, and that the disturbances dies out around this day. As the other plots from this experiment seem reasonable, not much focus will be put on this behaviour. Based on values at day 10 and 29, the decay constant, λ, is estimated to $8.4 \cdot 10^{-4}$ day^{-1} and the half-life to 2.3 years.

Fig. 4.13 shows the average concentration of the dissolved oxygen above 100 m depth (solid line) and below 300 m depth (dashed line), in the areas beyond the sill. In the basin, as seen in the previous experiments, there is a decay. However, in the top layer, there is a growth. The average concentration of dissolved oxygen goes from a value of about 5.1 ml/L to 5.5 ml/L in these 29 days. This is the effect of the fresh water entering the fjord through the rivers.

In Fig. 4.14a, the concentration field of dissolved oxygen is shown at day 29. In the top

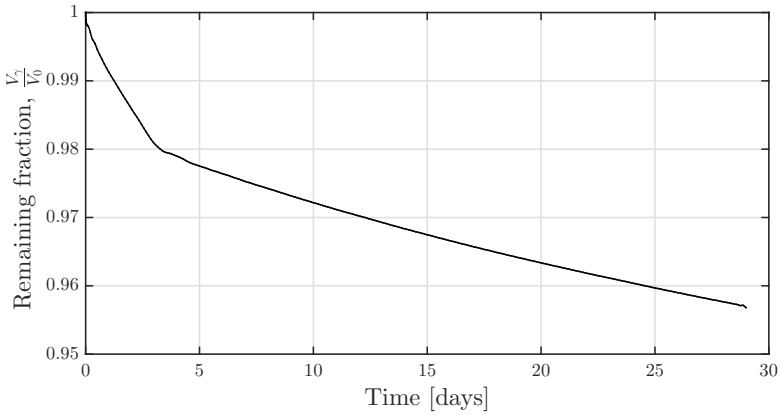

Fig. 4.12. The remaining fraction of marked bottom water below 300 m relative to its initial value, $\frac{V_\gamma}{V_0}$, plotted against time.

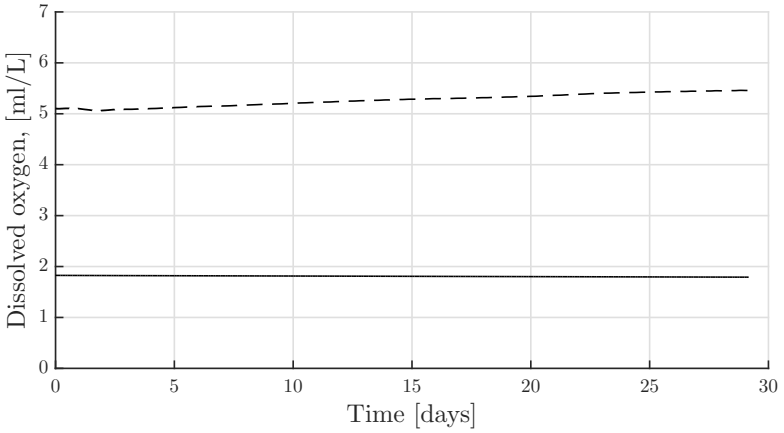

Fig. 4.13. The evolution of the average oxygen concentration below 300 m depth (solid line) and above 100 m depth (dashed line).

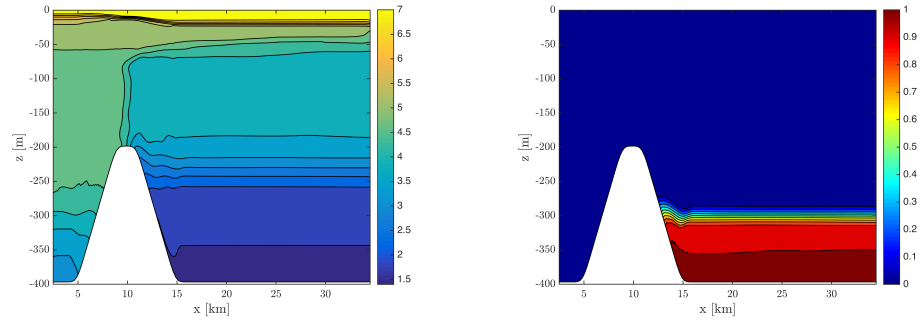

(a) (b)

Fig. 4.14. Contour of (a) the dissolved oxygen and (b) the passive tracer after 29 days of simulated time. The plane is a cross section through the y-directional centre.

layer, the levels of dissolved oxygen are higher. Elsewhere, it is similar to the contours from the two preceding experiments. The concentration field of the tracer, Fig. 4.14b, is almost identical to the plot from the previous experiment at the same time. This supports the assumption of the river runoff not affecting the circulation of the basin water. The curvy behaviour of the contour lines near the sill is also visible here.

No long run was performed for this experiment, as it produced similar results to the experiment with only tidal. One can assume that the half-life based on values at day 10 and 175 for this case would be similar to the one in the previous experiment.

4.4 Summary of preliminary experiments

The preliminary experiments indicated that longer run time probably should be used for the main experiments, as it gave other results. Based on the shorter simulations, of ca. 29 days, a half-life of 2 years and a few months was estimated. However, the longer simulations predicted a half-life of about 4 years.

The effects the tide and river had on the exchange of the basin water were negligible, in fact the experiments with tidal force and river runoff predicted a longer half-life than the experiments without.

5. Exp. 1: Four outlets of 0.25 m^3s^{-1}

Outlets were placed in the basin as an attempt to create artificial upwelling. The set-ups of the outlets for this experiment are given in Table 5.1. The specifications of the fresh water exiting the outlets are the same as described in Table 4.1. As the preliminary experiments showed, the results from the long runs (175 days) were different than the shorter runs (29 days). A simulation time of 175 days was thus chosen for the main experiments.

Outlet number	Location (i, j)	Flux [m^3s^{-1}]
1	(100, 4)	0.25
2	(100, 5)	0.25
3	(101, 4)	0.25
4	(101, 5)	0.25

Table 5.1. Set-ups in Exp. 1 for the outlets of fresh water at the bottom of the basin.

The outlets were located at the bottom, approximately in the centre of the fjord basin. They were spread over an area of four grid cells, 250 000 m^2. The vertical velocity of the water entering the fjord is relatively small, $4{\cdot}10^{-6}$ ms^{-1}, which indicates that this is primarily a buoyancy driven process (Fischer et al., 1979).

5.1 Evolution of the marked basin water

Fig. 5.1 shows how the amount of marked water below 300 m, V_γ, evolves in time. There is first a period of decay for the first 100 days and the first 70-80 of these might fit an exponential decay model. From day 100 a period of stagnant behaviour lasts until day 145-150, when a new decay begins. These periods will be denoted as Stage I, Stage II and Stage III.

The method of calculating half-life, as presented in chapter 3, is not straightforward to do for these results, as they do not fit to an exponential decay model. Fig. 5.1 shows that about 70 days is needed for the basin water to be reduced to its half. The decay rate changes shortly after this, making it hard to predict a half-life valid for all times. This shows that a half-life as defined in equation (3.9), is not possible to determine for this experiment. Plots of the concentration field for the tracer will be presented later

in the chapter, to examine where the marked water has been transported.

The average concentration of dissolved oxygen will be studied in the next section, as the actual motivation for this study is to see if the concentration in the depths can be increased.

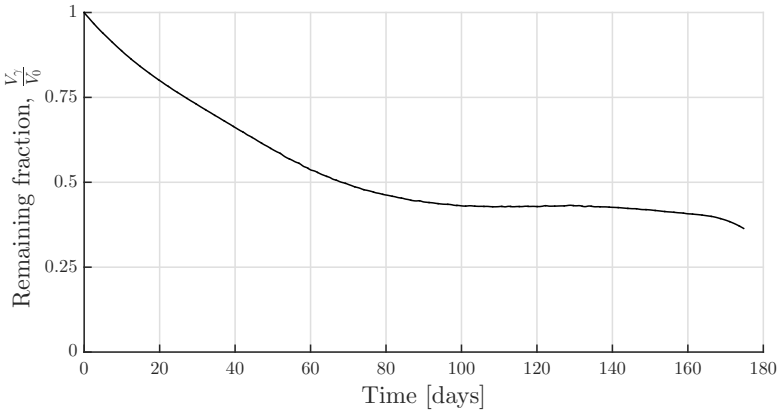

Fig. 5.1. The remaining fraction of marked bottom water below 300 m relative to its initial value, $\frac{V_\gamma}{V_0}$, plotted against time.

5.2 Evolution of the dissolved oxygen

Fig. 5.2 shows the evolution of the average concentration of dissolved oxygen in the top and lower 100 m in the area of the fjord beyond the sill.

In the top 100 m, the average concentration improves for the first 100 days, and then seems to stabilize around an average concentration of 6 ml/L. The first 29 days of this graph is similar to the results from the preliminary experiment with river runoff. The increase of the concentration in the top layer is therefore most likely caused by the river.

The concentration of dissolved oxygen in the depths of the basin seems to improve as well, but it takes some time before a change is visible. In the beginning, the average concentration is nearly constant, a little below 2 ml/L, which is defined as hypoxia. After about 60 days, a growth begins. Around day 100, the average concentration exceeds 2 ml/L, and the growth continues.

Around day 170, near the end of the simulation, a new growth rate is visible. This has a similar shape to the one at the same time in Fig. 5.1, except they point in opposite directions, which is reasonable; when the marked water is transported out of the depths, the hypoxic water is also transported out, and more saturated water can replace it. The

tracer concentrations decreases and the oxygen concentrations increases.

In the next section, concentration fields of the dissolved oxygen and the tracer will be presented.

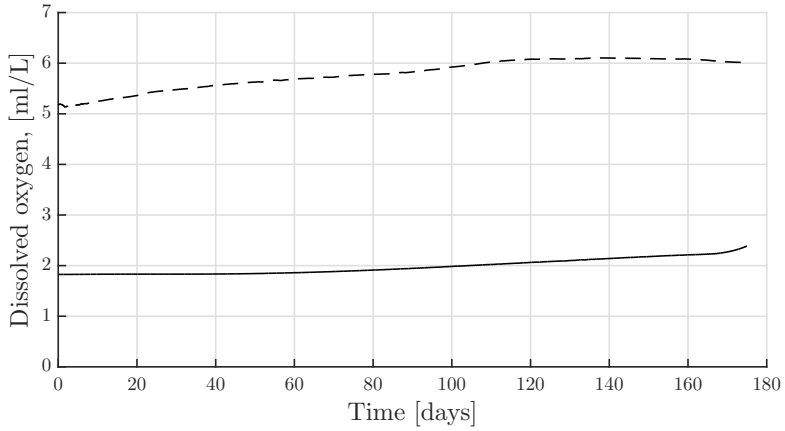

Fig. 5.2. The evolution of the average oxygen concentration below 300 m depth (solid line) and above 100 m depth (dashed line).

5.3 Concentration fields of the passive scalars

Fig. 5.3 shows the concentration fields of the dissolved oxygen and the tracer after 30, 100, 145 and 175 days of simulated time. The left column shows the concentrations of the dissolved oxygen and the right column shows the concentrations of the tracer.

The fresh water discharge will move upwards through the ambient water mass as a buoyant plume. As the bottom water is entrained into and transported up by the buoyant plume, water are descending on both sides, filling the basin with more saturated water. It seems as though the plume reaches its height early in the simulation, and then expands in the horizontal directions rather than the vertical.

Fig. 5.3 (a-b) shows the concentration fields at day 30. The contours indicates that the top of the plume are at, or a bit above, sill level. There are mainly high (low) concentrations of the tracer (dissolved oxygen) in the plume, and they are distributed in a pyramid-shape in the plume, i.e. the width of the plume decreases with its height.

The concentration fields at day 100 of the simulation is shown in Fig. 5.3 (c-d). At this time, the top of the plume is clearly above sill level. The contours shows that the concentrations of dissolved oxygen in the plume still are at the lowest level, and that the concentration of the passive tracer decreases with the plumes height. The width

of the plume has grown, and it now largest near the top of the plume, with decreasing width towards the bottom.

At day 145, Fig. 5.3 (e-f), the sides of the plume has descended and the width of the plume is now somewhat constant through the plume. Near the top of the plume, it is a little wider. The axis of the discharge works as a barrier since there is an upward velocity here; this separates the plume. The left side of the plume is wider than the right side, and the highest concentrations of the tracer are visible at the right side. This may be due to the fact that the right side of the plume is physically blocked by the axis of the discharge and the eastern boundary.

Towards the end of the simulation, in Fig. 5.3 (g-h), the right side of the plume is transported horizontally and a little upwards. The left side of the plume seems less wide than at day 145. In the concentration field of the dissolved oxygen, higher concentrations are visible near the top of sill. It may be that the plume has mixed well with the ambient water from day 145 to day 175, and hence reduced the visible width of the left side of the plume.

These two passive scalars reflects the velocity field, since the same equation govern their transport. The terms in this equation are the advection by the velocity field, and the vertical and horizontal diffusion. In this study, the passive scalars are transported by the velocity field in addition to the vertical diffusion.[1] In the next section, the horizontal and vertical velocity fields will be studied.

5.4 Velocity fields

Fig. 5.4 shows the x-and z-component of the velocity field on day 30, 100, 145 and 175 of the simulation. The left column shows the horizontal component and the right column shows the vertical component. To focus on the velocities near the discharge, the plume and the sill, only the velocities below 160 m is plotted.

Studying the horizontal velocity field, three features stand out: i) Near the bottom, where the discharge is located, the horizontal velocities indicate a stream towards the discharge from both sides, converging. ii) Higher up, there is an area where the horizontal velocities move away from the centre of the plume, diverging. iii) On the left side of the sill, the horizontal component indicates outflow, negative value, or inflow, positive value.

[1] $A_H = 0$, so there is no horizontal diffusion.

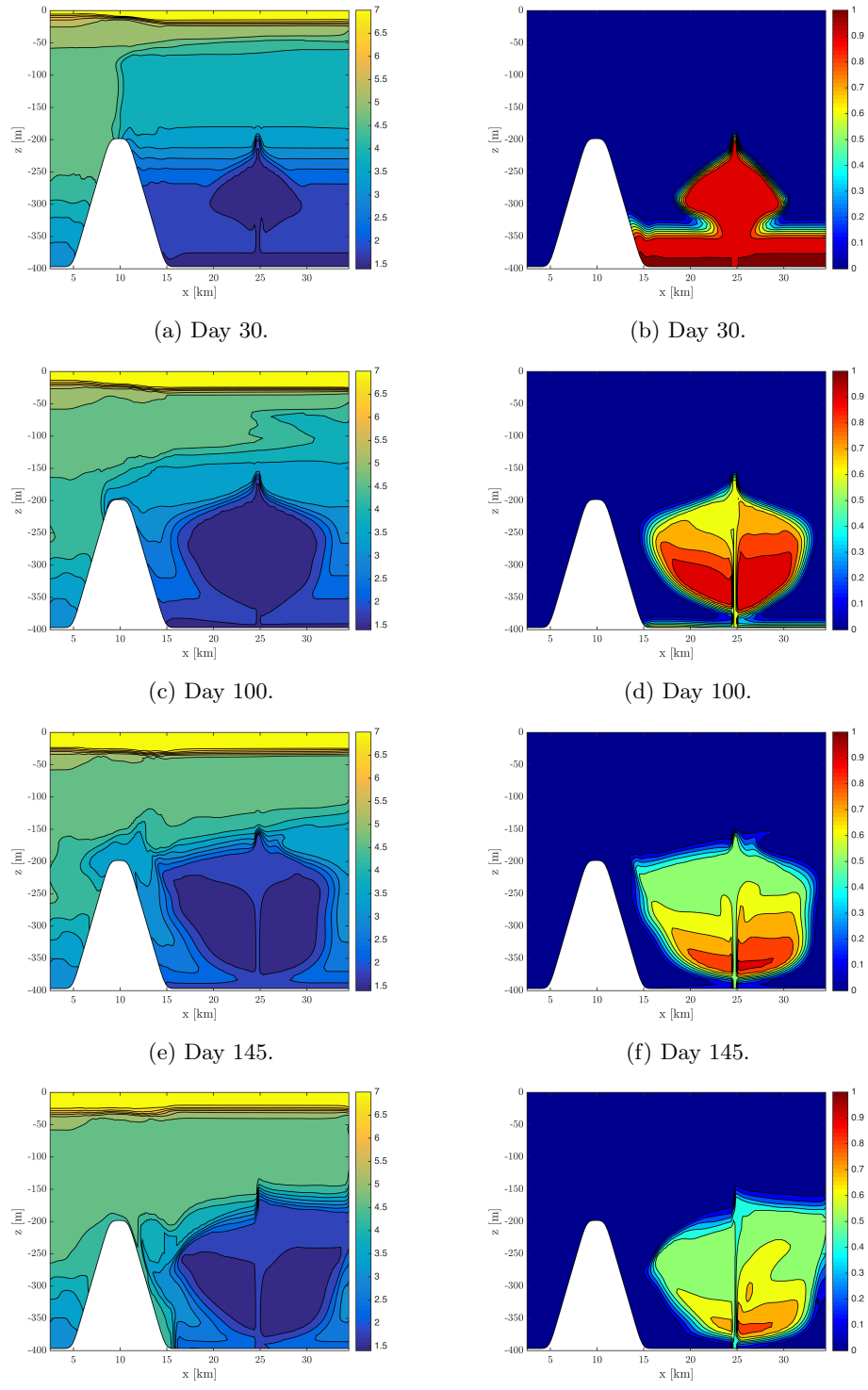

(a) Day 30.

(b) Day 30.

(c) Day 100.

(d) Day 100.

(e) Day 145.

(f) Day 145.

(g) Day 175.

(h) Day 175.

Fig. 5.3. Contour of the dissolved oxygen [ml/L] (left column) and the passive tracer (right column) after 30 (a-b), 100 (c-d), 145 (e-f) and 175 (g-h) days of simulated time. The plane is a cross section through the y-directional centre.

In all the plots of the horizontal velocity component in Fig. 5.4, the first feature is visible, but the magnitude of the velocities varies. In all of the basin area below a depth of 350 m, the velocities points towards the discharge. The velocities are highest near the discharge.

The second feature is visible at day 30, 100 and 145, in Fig. 5.4 (a, c, e), but the vertical placement of the divergence area varies and ranges from a bottom point of 300 m to a top point of 160 m depth. The magnitude of the velocities varies as well. This divergent area explains why the plume spreads in the horizontal direction here, and has a top point around 200 m depth. At day 175, there are generally higher velocities visible in larger areas of the domain. There is no clear divergence area, but the positive velocities between 200 m and 300 m depth on the right side of the basin supports the shape of the plume, directed towards the right, seen in Fig. 5.3 (g-h).

The third feature is visible at day 30, 100 and 145. At day 30 and 100, an outflow through the open boundary is visible, and at day 145 there is an inflow. The same direction of the velocity is found above the sill and on the right side of it. This is most likely governed by the tide.

At day 175, in Fig. 5.4g, on the right side of the sill, in the area close to the bottom/slope, the horizontal velocities are positive. At the same time, in Fig. 5.4h, the vertical velocities are negative in the same area. The velocity fields at this time indicates an inflow over the sill and towards the bottom of the basin.

In the vertical velocity fields, in Fig. 5.4 (b, d, f, h), the upwelling area above the discharge is visible. The vertical velocities are greater then the discharge velocity, indicating that the plume is accelerated due to buoyancy forces. There are smaller velocities pointing downwards at both sides of the discharge. At both sides of the sill, there are higher vertical velocities than in the rest of the domain, except for the upwelling area. The directions of the vertical velocities along the slopes of the sill are connected to the horizontal velocities there. When there is an inflow, water flows over the sill and must have a positive vertical velocity on the left side, and opposite on the right side. For outflow, the directions are reversed.

The next section will present density distributions in the same areas as the velocity fields were shown.

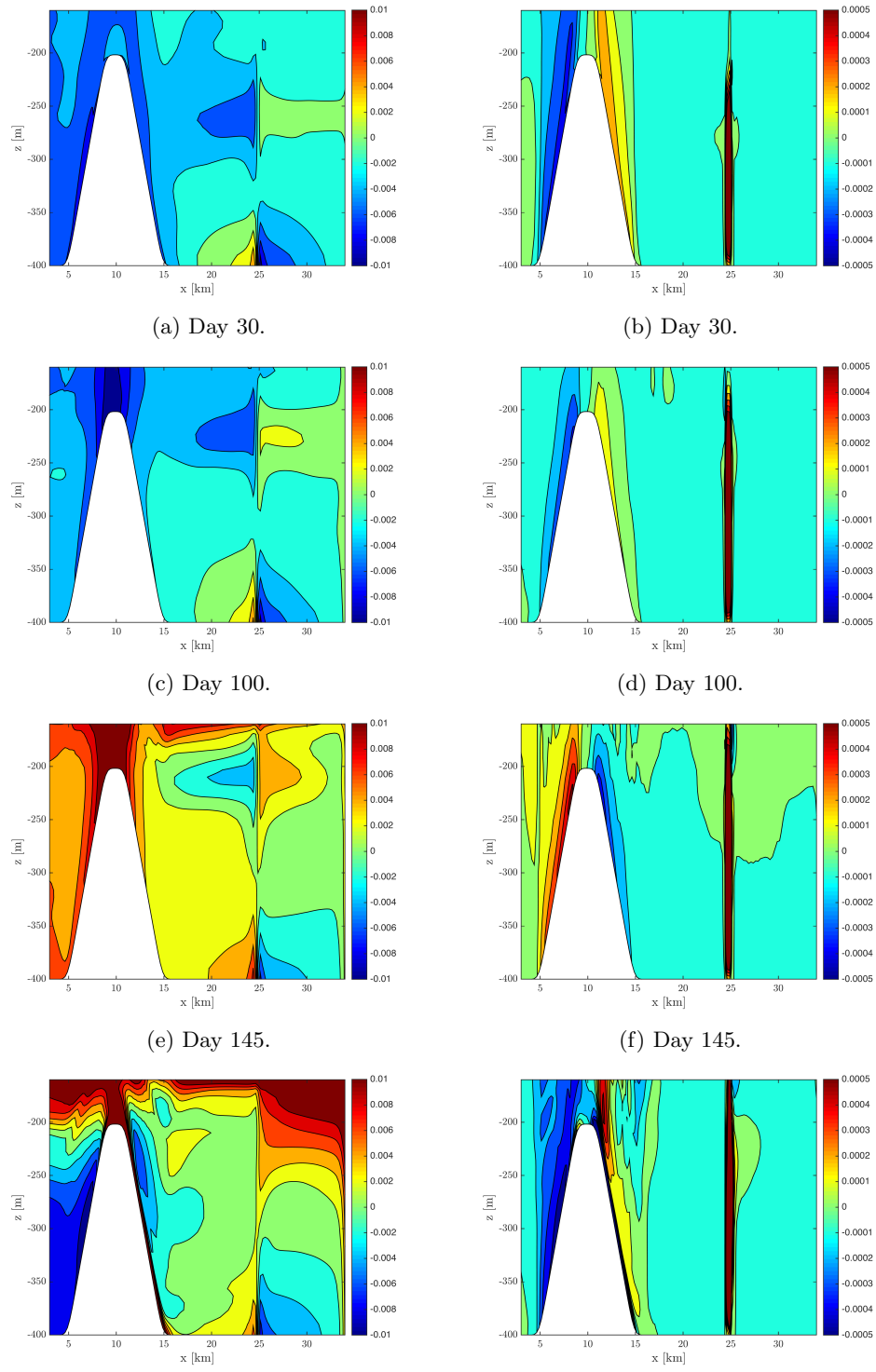

(a) Day 30.

(b) Day 30.

(c) Day 100.

(d) Day 100.

(e) Day 145.

(f) Day 145.

(g) Day 175.

(h) Day 175.

Fig. 5.4. Contour of the horizontal velocity component, U [ms^{-1}] (left column), and the vertical velocity component, W [ms^{-1}] (right column). The contour spacings are $2 \cdot 10^{-3}$ ms^{-1} for U and $1 \cdot 10^{-4}$ ms^{-1} for W.

5.5 Density

Fig. 5.5 shows the density distribution below 160 m depth at days 30, 100, 145 and 175. The top 160 m is excluded because the density differences near the sill depth and in the basin are of interest.

The density distribution is visualised by the contour lines, or isopycnals, of chosen density values. In the area between these lines, the density of the fluid ranges between the values of the surrounding isopycnals. When discussing the density distribution, the areas between isopycnals will sometimes be referred to as *density layers*, even though they are not actual layers of the same density, but describes the density range of that water.

The fresh water discharge mixes with the ambient, denser water and rises due to buoyancy. When the plume experiences neutral buoyancy it diverges laterally at a depth of intrusion (Fischer et al., 1979; Malin, 1989). In Fig. 5.5 (a-d), vertical isopycnals is seen at both sides of the bottom outlet as they continue up until a depth where they bend horizontally towards the sill or the eastern boundary. Some disturbances in these isopycnals are also seen. The rising plume is visible as the fluid between these vertical isopycnals. Intrusion depth is thus somewhere in the density layer corresponding to the density of the buoyant plume. This area will for simplicity be denoted as the *intrusion layer*. The exact depth is not possible to see, since the intrusion layer span a vertical length of 50 m to 100 m.

In Fig. 5.5 (a-c), a clear peak in the upper isopycnal of the intrusion layer is seen. This could be caused by the momentum of the rising plume. As the plume rises, it accelerates due to the buoyancy force. It reaches the point of negative buoyancy at this interface, and loses its momentum. In Fig. 5.5 (c-d), disturbances in the isopycnals other than the peak of the plume is visible. These disturbances or perturbations of the isopycnals results in internal waves (Kundu et al., 2016).

In time, the density inside the basin is reduced. This results in a difference between the stratification of the outside water and the basin water. High-density intrusion can be observed at day 175, in Fig. 5.5d, as the water on top of the sill has a higher density than the water at the same depth but beyond the sill. The isopycnal above the sill follows the slope to a depth of 300 m where the isopycnal of the same value is located inside the basin. This indicates that water with a slightly greater density descends from the top of the sill, along the slope and down into the basin, to a depth of 300 m or

greater.

The density gradient inside the basin is reduced in time. This is visible by the increased vertical distance of the isopycnals.

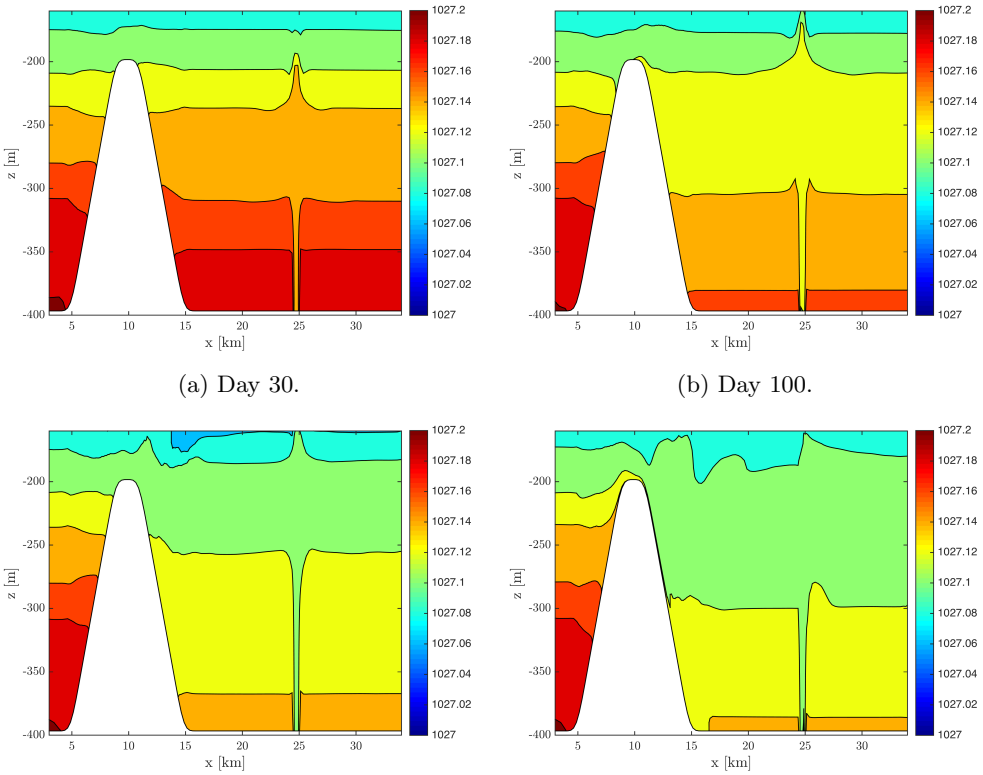

(a) Day 30.

(b) Day 100.

(c) Day 145.

(d) Day 175.

Fig. 5.5. Contour of the density, ρ [kg/m^3], at day 30, 100, 145 and 175, with a contour spacing of 0.02 kg/m^3. The upper 160 m is omitted to better illustrate the density differences in the basin and near the sill.

5.6 Turbulent vertical mixing

Fig. 5.6 shows the vertical eddy diffusivity coefficient, K_H, for two different times of the simulation. Since the values of K_H ranges from the minimum value of $O(10^{-5})$ to $O(1)$, a log-scale was chosen.

The vertical eddy viscosity coefficient, K_M, is not plotted. Since these coefficients are evaluated by equations (2.25) and (2.26), and proportional to the product ql the two stability functions, S_M and S_H, the vertical profiles are almost proportional. The profile of K_M would thus have a similar shape.

Data from three vertical lines are plotted against the depth, z. The dotted line is taken from the grid cell specified by indices $(i, j) = (100, 4)$. The solid line is taken from the another outlet cell, with $(i, j) = (101, 4)$ and thus to the right of the dotted line. The dashed line is taken from the cell to the right of the outlet, specified by $(i, j) = (102, 4)$

Fig. 5.6 illustrates that K_H, and so the turbulence kinetic energy and turbulence length scale, is highest in the area just above the outlet cells, and mainly below sill depth, 200 m. The dashed line is mostly equal to the minimum value of K_H, $2 \cdot 10^{-5}$. The production of turbulence kinetic energy depends on the balance between vertical shear and stratification. Outside the plume, water is stratified, the shear is weak and the production of turbulence kinetic energy is weak, this gives minimum values of K_H. This indicates that the turbulent effects of the outlets are limited to the area above the outlets. At day 30, the K_H has a minimum values above 200 m depth. At day 100, K_H has values above the minimum in the top 25 m. This is equal for all three lines, and is probably caused by the current induced by the river runoff.

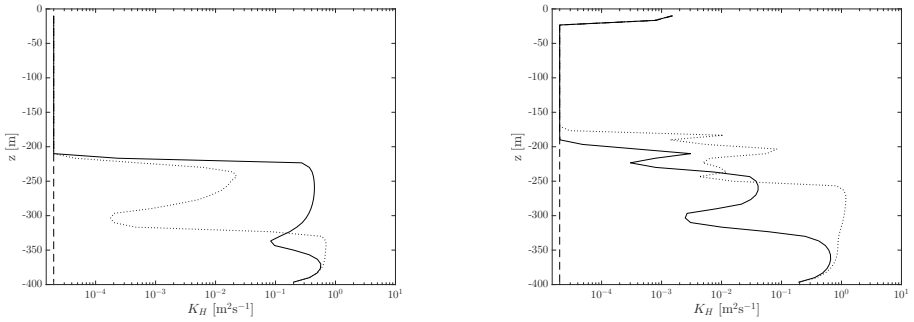

(a) Day 30. (b) Day 100.

Fig. 5.6. The vertical variation of the vertical eddy diffusion coefficient, K_H [m^{2}s^{-1}], plotted on a log-scale at day 30 and day 100. Data is collected from vertical lines where the j-coordinate is 4 and the i-coordinate is 100 (dotted line), 101 (solid line) and 102 (dashed line).

The unstable, or turbulent, areas can be visualised by areas where Richardson number has a critical value. The Ri number was calculated by equation (2.17), and areas where Ri is below the critical value are marked red in Fig. 5.7. Green areas are stable areas, where the Ri-number is above the critical value. In the beginning, it is only the area above the outlet and approx. 200 m upward where the Ri-number is below its critical value, see Fig. 5.7a. Later on, in Fig. 5.7 (b-d), there is another area where the Ri-number are below the critical value. At the right side above the sill, there is a small area that develops to a bigger one from day 100 to day 175. This is about the same area as the disturbances in the isopycnals were seen.

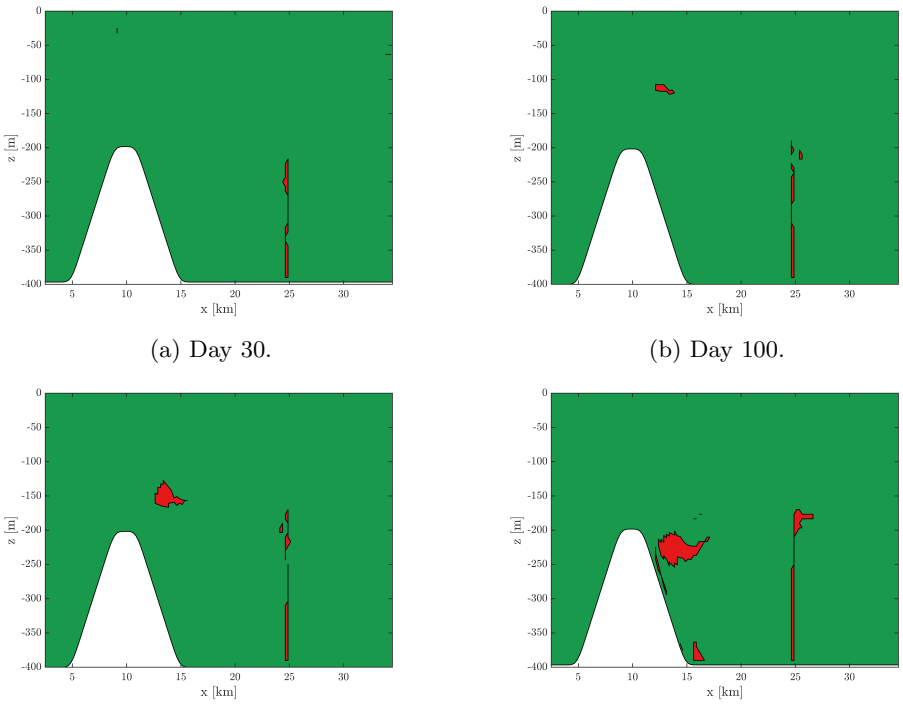

(a) Day 30.

(b) Day 100.

(c) Day 145.

(d) Day 175.

Fig. 5.7. Areas where the Richardson number is below (red) and above (green) its critical value, 0.25, through days 30, 100, 145 and 175.

5.7 Discussion

The three different stages identified in the evolution of V_γ, can be explained by the other results presented in this chapter.

In the first 100 days, most of the deepest portion of the basin water is lifted up by entrainment with the discharge. This reduces V_γ and gives the exponential decay seen in Stage I. The inflowing water replacing the rising bottom water has a tracer concentration of zero. For the dissolved oxygen however, the inflowing water has a low, nearly equal concentration as the ascending fluid. The result is that the concentrations of dissolved oxygen below 300 m seem constant for these first days.

Stage II follows with a nearly constant value of V_γ. There is a combination of two attributes that possibly causes this. Firstly, the ambient water being entrained and transported by the plume has lower tracer concentrations, since the highest concentrations have been transported up by the plume, and is no longer in the area where entrainment happens. This reduces the flux of the tracer out of the area below 300 m. Secondly, both sides of the plume descends from day 100 to day 145. This gives a flux of the tracer back into the lower 300 m. If the tracer flux out and in of the area below 300 m are nearly equal, this would explain the nearly constant value of V_γ.

Around day 145-150, a new period of decay was identified, Stage III. From day 145 to day 175, the concentration fields illustrated that the concentration of the tracer below 300 m was reduced. This explains the decay of V_γ between in this period. From the density field and plot of areas with critical Richardson number, instabilities could be detected on the right side of the sill. The high-density intrusion brings water with a low concentration of the tracer and higher concentration of the dissolved oxygen. This could result in a decrease of V_γ and an increase of the concentration of dissolved oxygen below 300 m.

The fresh water discharge at the bottom is a represents a constant supply of available potential energy to the system (Fischer et al., 1979). Some of this energy is transformed to kinetic energy as the fluid is accelerated. A fraction is used to create internal waves, which consist of both potential and kinetic energy. At the side wall, these waves are purely reflected. At the sill, however, these internal waves can propagate up and down the slope or break and cause irreversible mixing (Gill, 1982). Energy can also be transformed as irreversible mixing when the buoyant plume rises. The detailed study of these energy transfers are beyond the scope of this thesis.

6. Exp. 2: Four outlets of 2.5 m^3s^{-1}

The flux of each of the outlets were increased by a factor of ten. Besides that, the set-ups were equal to the ones in Table 5.1. The vertical velocity from the outlet was in this experiment 10 times higher, $4{\cdot}10^{-5}$ ms^{-1}, which still is small. The processes are thus mainly buoyancy driven (Fischer et al., 1979).

6.1 Evolution of the marked basin water

The remaining fraction of marked basin water below 300 m, V_γ, as a function of time is shown in Fig. 6.1. The figure shows an initial sharp decline of the marked basin water below 300 m, where it reaches a local minima around day 24. The three stages of the evolution can be observed also in these results. First, there is a period of what could be exponential decay, denoted as Stage I in the previous experiment. In this experiment, Stage I lasts for about 24 days. Stage II follows. There is an increase and perhaps some stagnation before the decay continues around day 55. Stage III begins and the decay rate is closer to a linear than exponential. Approximately at day 100, the fraction of V_γ is again reduced to the same as the first minima. The decay continues for the rest of the simulation, with some disturbances on the curve between day 80 and 140.

After about 10 days, half of the original marked water have been lifted above 300 m depth. However, a half-life based on an exponential decay model can not be found since the decay rate varies non-exponentially. There is at least a great reduction of the marked basin water below 300 m. By the end of the simulation, 175 days of simulated time, the amount of the marked water below 300 m is reduced to less than 2% of the initial value.

6.2 Evolution of the dissolved oxygen

Fig. 6.2 shows the the average concentration of dissolved oxygen as a function of time below 300 m (solid line) and above 100 m (dashed line) depth, in the area beyond the sill.

In the top 100 m, the concentration increases and reaches a value of about 6 ml/L by the end of the simulation. There is a continuous weakly varying growth. Compared to

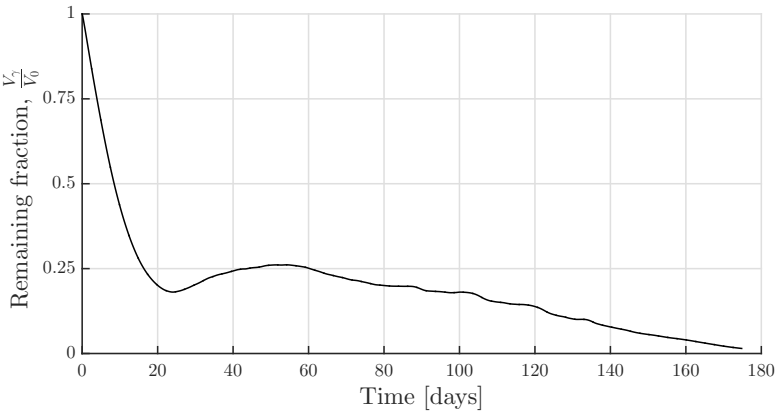

Fig. 6.1. The remaining fraction of marked bottom water below 300 m relative to its initial value, $\frac{V_\gamma}{V_0}$, plotted against time.

the same figure in Exp. 1, which stabilized around a value of 6 ml/L, there is less that indicates a stagnation in this figure. However, a limiting value is the concentration of dissolved oxygen in the river water, 7.5 ml/L.

In the bottom 100 m of the basin, there is mainly an increase in the concentration, but also a short period of decrease between day 35 and 55. The growth rate varies; in the beginning there is a relatively sharp growth, but after the period of decay, the growth rate is reduced. By the end of the simulation, the average concentration of dissolved oxygen below 300 m depth in the basin has reached a value of 4.5 ml/L and does not seem to stop at this value.

The concentration fields of the two passive scalars, the dissolved oxygen and the tracer, can be studied to see how these are transported through the simulation.

6.3 Concentration fields of the passive scalars

Fig. 6.3 shows the concentration fields of the dissolved oxygen and the tracer after 24, 50, 100 and 160 days of simulated time.

Fig. 6.3 (a-b) shows the concentration fields at day 24. This is the time when the first local minima in Fig. 6.1 is observed. The top of the plume, which is a small peak, is seen at a depth of approx. 100 m. The width is largest around 150 m depth, and decreases with depth. The highest concentrations of the tracer is found in the bottom part of the plume, and the lowest concentrations of dissolved oxygen is found nearly through the whole plume. The left side of the plume has a larger width and a shorter

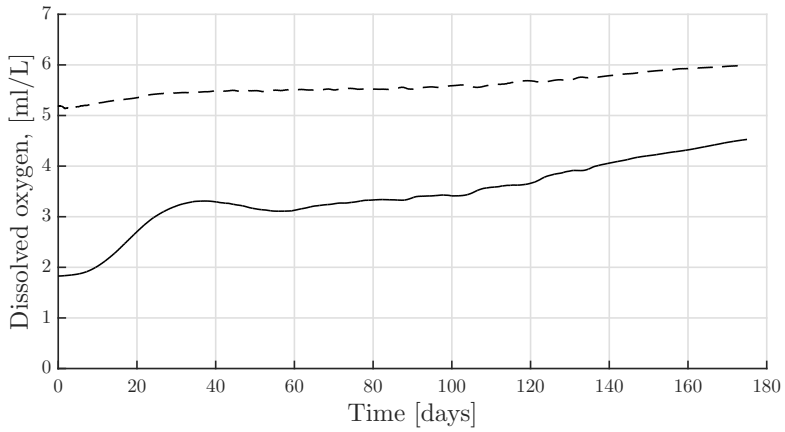

Fig. 6.2. The evolution of the average oxygen concentration below 300 m depth (solid line) and above 100 m depth (dashed line).

height than the right side. Apart from that, there seems to be symmetry about the axis of the discharge.

At day 50, Fig. 6.3 (c-d), the left and right side of the plumes appear different, the symmetry has vanished. The right side has an almost constant widht, while the left side has a larger and more varying width. The left side is stretched out over the sill and towards to the open boundary. The right side retains higher/lower concentrations of the tracer/dissolved oxygen than the left side. This is probably due to the fact that on the left side, the scalars are more diluted since they are spread over a larger area. On the right side, the water is locked between the closed boundary and the axis of the discharge. The top of the plume has the same location as at day 24, but the bottom has descended towards the basin floor.

Later on, at day 100, Fig. 6.3 (e-f), the shape of the contours are similar to those at day 50, but the concentrations of the tracer/dissolved oxygen are lower/higher.

At day 160, Fig. 6.3 (g-h), the original marked water is diluted to the point where nearly all of it has a concentration at the minimum contour level. The only areas where the contour shows concentrations of the tracer above the minimum value, are a small area to the right of the sill and a slightly larger area in the right side of the basin. The same applies for the concentration field of the dissolved oxygen; the lowest concentrations are found in those two areas. Nearly all of the hypoxic water is removed from the basin at this time.

In the next section, the horizontal and vertical velocity components will be studied for

various times.

6.4 Velocity fields

Fig. 6.4 shows the fields of the horizontal and vertical velocity components, in the left and right column, respectively. The figure shows velocities at days 24, 50, 100 and 160.

The lateral convergence and divergence zones, as described in the previous chapter, are also visible in these velocity fields. In Fig. 6.4 (a, c, e), the convergence area towards the outlet is seen. The velocities are highest near the discharge, but they point towards the plume in the whole basin area below 300 m depth. At day 160, in the horizontal field, there are almost only positive velocities, and those that are negative, are small in magnitude. The area in the bottom 300 m of the basin could be a convergence, especially if observing the left side. On the right side, there are small velocities, and negative velocities between approx. 300 m to 350 m depth.

In Fig. 6.4 (a, c), the area of lateral divergence ranges from about 200 m to 100 m depth. According to this, the plume spreads horizontally above the sill depth at these times. At day 100, Fig. 6.4e, the area between 200 m to 100 m depth could be a divergence area. The velocities point in opposite directions and away from the plume, but the regions are not as clear as in the two previous times. There is a relatively large negative velocity, an outflow, above the sill. This corresponds well to the concentration fields seen at the same time, where they were seen transported out over the sill.

Along the top of the sill, there is a positive and horizontal velocity at at all times shown in Fig. 6.4. The same velocity is seen along the right side of the sill, indicating a flow across the sill and down into the basin, following the bottom. At day 24, it is confined to a area close to the bottom, but in time the area grows. The magnitude is above the highest contour level, higher than 0.03 ms^{-1}.

Above the discharge, the vertical velocity is positive for all the times shown in the right column of Fig. 6.4. On both sides of the rising plume, the vertical velocity components are small and negative, except for day 160, in Fig. 6.4h, where small positive values are seen. Larger positive and negative velocities are seen along the sides of the sill, depending on the direction of the horizontal velocity. Along the right slope of the sill, near the bottom, the velocity is negative in all the vertical velocity fields shown. However, in Fig. 6.4 (f, h) the vertical velocity is positive some σ-layers above.

The values of the velocity components at the sill top and along the slope towards the

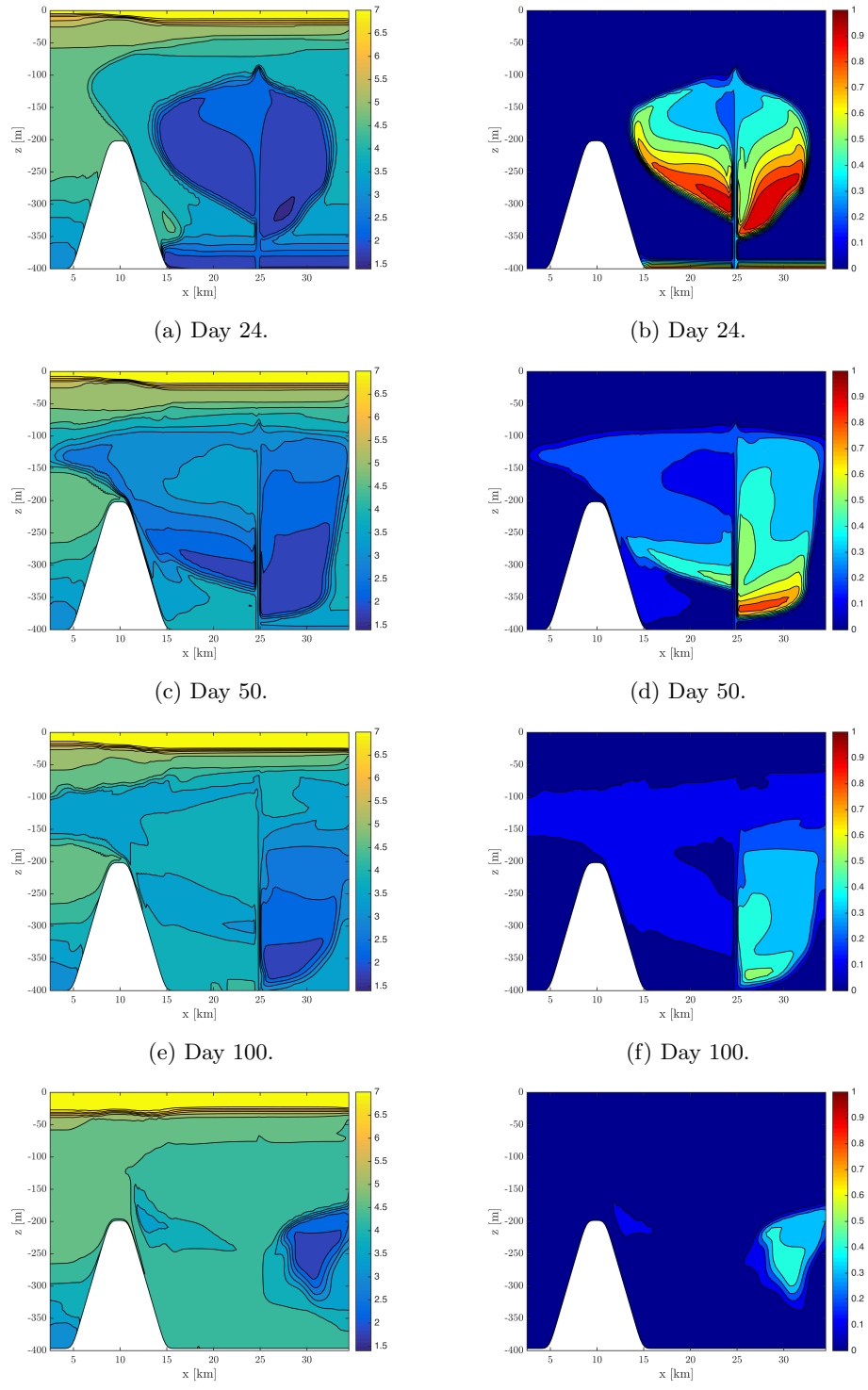

(a) Day 24.

(b) Day 24.

(c) Day 50.

(d) Day 50.

(e) Day 100.

(f) Day 100.

(g) Day 160.

(h) Day 160.

Fig. 6.3. Contour of the dissolved oxygen [ml/L] (left column) and the passive tracer (right column) after 24 (a-b), 50 (c-d), 100 (e-f) and 160 (g-h) days of simulated time. The plane is a cross section through the y-directional centre.

basin, indicates an inflow over the sill. This could indicate high-density intrusion. In the next section, the density distribution will be studied.

6.5 Density distribution

In Fig. 6.5, the density distribution below 100 m depth is shown at different times of the simulation. This area was chosen to include the areas where the plume of the passive scalars was observed in previous plots.

After 10 days, the stratification inside the basin has changed, see Fig. 6.5a. The isopycnal of the heaviest water, seen outside the sill, is no longer visible inside the basin. In time, Fig. 6.5 (b-d), the density of the basin water is reduced, as the water with highest density is entrained into the plume and rises. This again creates a lower density of the plume, since the ambient fluid it is entrained with now has a lower density than before. This process continues through days 54 and 100 as well. Water gradually sinks down on both sides of the discharge, and the density in the basin decreases. From day 100 to day 125, this is reversed. Heavier water has returned to the basin, through high-density intrusion along the sill. From day 125 to 175, more of the denser water has entered the basin.

The isopycnals are gradually more disturbed. In a stable, stratified field the isopycnals are horizontal. In the beginning, there are smaller disturbances, and the peak is seen where the buoyant plume is decelerated. In time, the disturbances grow in amplitude and can be seen as sharp peaks along many of the isopycnals. These disturbances are a sign of the energy in the system, as discussed briefly in the previous chapter. With a ten times higher flux of fresh water, more potential energy is constantly put into the system.

6.6 Turbulent vertical mixing

The turbulent vertical mixing are visualised by plots of the vertical eddy diffusivity coefficient, K_H, and areas where the Richardson number is below its critical value.

Fig. 6.6 shows values of K_H along three vertical lines, the same as in the previous experiment, at day 30 and day 100. There are relatively large values up to 100 m depth, and a little above. In the top 25 m, in Fig. 6.6b, K_H has a higher value than the minimum, probably caused by the river. The turbulence kinetic energy and turbulence length scale is thus larger in the vertical column above the discharge up until

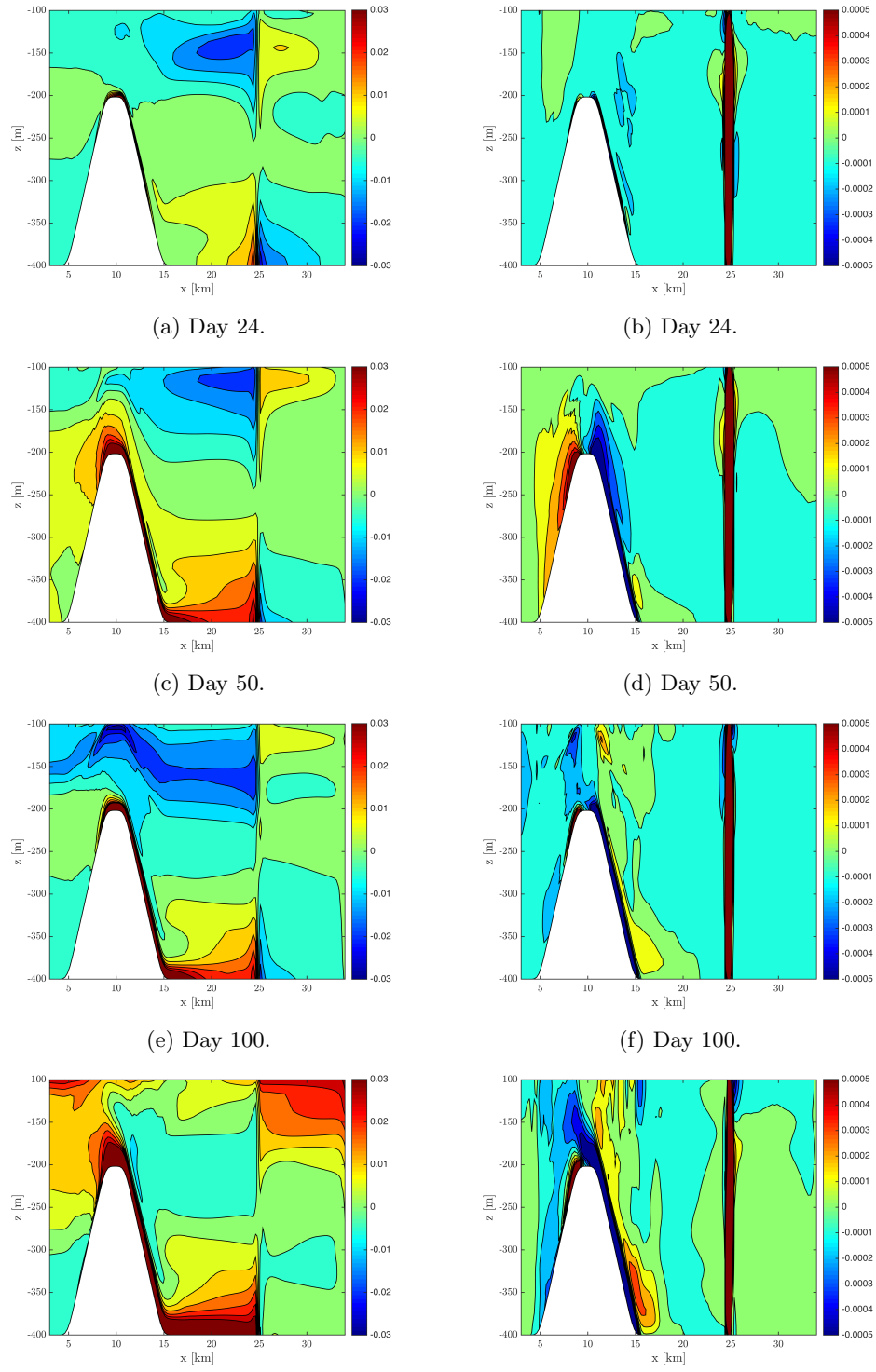

(a) Day 24. (b) Day 24.

(c) Day 50. (d) Day 50.

(e) Day 100. (f) Day 100.

(g) Day 160. (h) Day 160.

Fig. 6.4. Contour of the horizontal velocity component, U [ms^{-1}] (left column), and the vertical velocity component, W [ms^{-1}] (right column). The area is a vertical plane through the y-directional centre. The top 100 m is omitted. The contour spacings are $5 \cdot 10^{-3}$ ms^{-1} for U and $1 \cdot 10^{-4}$ ms^{-1} for W.

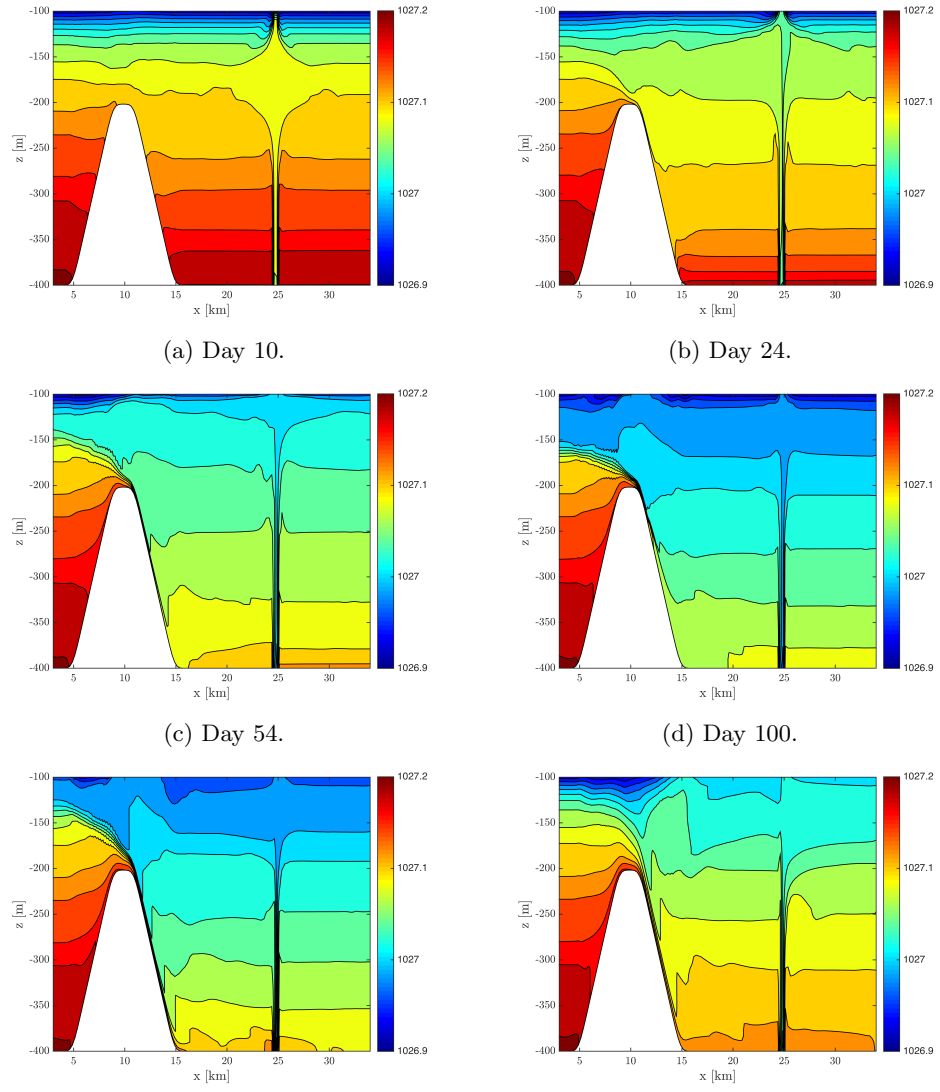

(a) Day 10.

(b) Day 24.

(c) Day 54.

(d) Day 100.

(e) Day 125.

(f) Day 175.

Fig. 6.5. Contour of the density, ρ [kg/m^3], at day 30, 100, 125 and 175, with a contour spacing of 0.02 kg/m^3. The upper 100 m is omitted to better illustrate the density differences around the plume.

100 m depth. At day 100, the dashed line, representing the grid cell to the right of the discharge, has some values above its minimum. The turbulence kinetic energy in the top 25 m, gives an equal value of K_H for all three lines. This supports the suggestion that this is caused by the river produced current, since it apparently is independent of the location of the discharge and is equal for this experiment and Exp. 1.

Fig. 6.7 illustrates areas where the Richardson number is above (green) and below (red) its critical value, 0.25, through days 10, 100, 125 and 175. At first, in Fig. 6.7 (a-b), the areas of critical Ri number are limited to a vertical column above the discharge, ending at around 100 m depth. Small areas along the right side of the sill are also seen. Later on, in Fig. 6.7 (c-d), the areas of critical Ri number along the sill grows in size. There are also critical values on the left side of the sill, but over a smaller area. An area of critical Ri number is also observed 100 m to 50 m above the sill, to the right. These areas are the same as where the isopycnals grew uneven and had peaks, and could be assumed to be unstable.

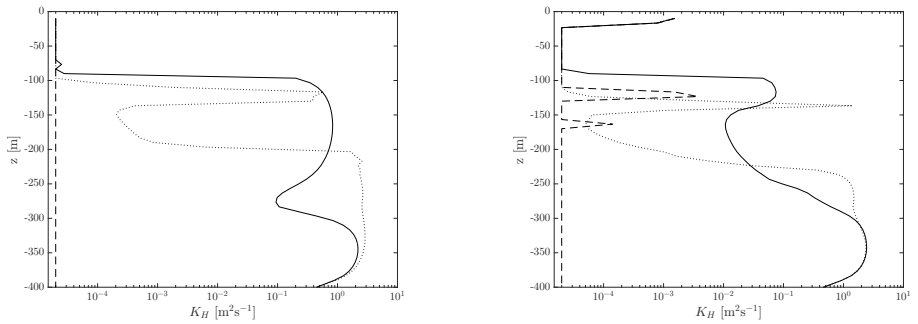

(a) Day 30. (b) Day 100.

Fig. 6.6. The vertical variation of the vertical eddy diffusion coefficient, K_H [m^{2}s^{-1}], plotted on a log-scale. Data is collected from vertical lines where the j-coordinate is 4 and the i-coordinate is 100 (dotted line), 101 (solid line) and 102 (dashed line).

6.7 Discussion

In this experiment, as well as in Exp. 1, three stages were identified. First there was Stage I, where an exponential decay model could fit the results. The fresh water flux of 10 m^{3}s^{-1} results in a lesser density in the buoyant plume, compared to Exp. 1. This results in a depth of intrusion higher up than in Exp. 1. The velocity fields showed a divergence zone located mainly above sill level. Since the scalars are transported farther up and at a higher rate, it is not surprising that the decay rate is higher for this simulation.

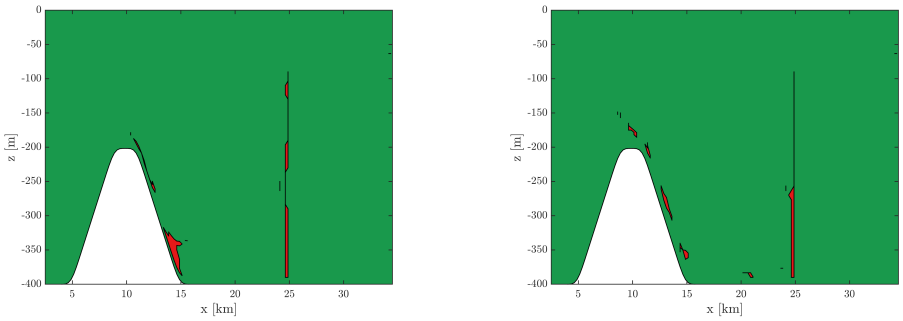

(a) Day 30.

(b) Day 50.

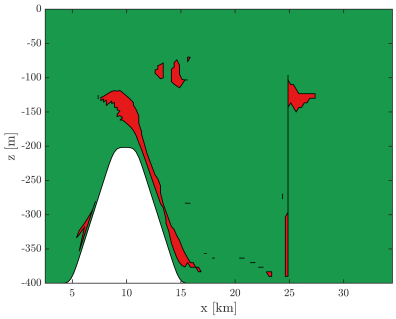

(c) Day 125.

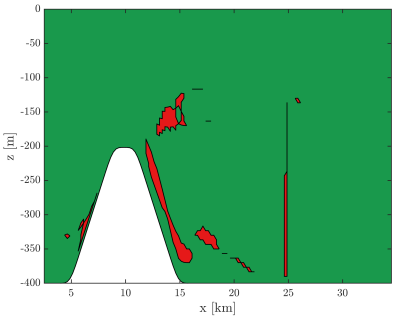

(d) Day 175.

Fig. 6.7. Areas where the Richardson number is below (red) and above (green) its critical value, 0.25.

The decay period lasted until day 24, where a local minima of V_γ was found. At this time, less than 0.2 of the original marked water remained below 300 m. A concentration field of the tracer at this time showed that a great deal of the marked water above the depth of 300 m, although most of it was still within the basin. This could be a weakness of this method of measurement, as it only tells us the amount of tracer water below 300 m depth of the basin. By studying the concentration fields, the velocity fields, the density distribution and the turbulent vertical mixing, more details are given. This is in general a good reason for having both quantitative and qualitative methods for the analysis; they complement each other.

Stage II, a period of increase and stagnation of V_γ, continued and lasted until day 55. In the density distribution and the velocity fields, it is visible that the physical process is mostly similar to other times. The convergence towards the discharge, the rise of the buoyant plume and the divergence at the depth of intrusion. The reason for the increase in V_γ is that the tracer flux into the depths of the basin are greater than the flux up through the plume. Parts of the bottom water has been recycled; rising up with the buoyant plume, diverging laterally and descending down into the basin.

In Stage III, there is a continuing decay of V_γ. There are some small disturbances on the curve between day 80 to 140. This suggests that the difference between the flux of the tracer into and out of the bottom 300 m is varying. The disturbances in the isopycnals, or the internal waves, in combination with the high-density intrusion, can be a source of the oscillations seen in the graph of $\frac{V_\gamma}{V_0}$. The downward velocity can vary, as well as the tracer concentration of the water being transported into and out of the basin depths.

7. Exp. 3: One outlet of 1 m^3s^{-1}

A new experiment with the same flux as the first experiment, 1 m^3s^{-1}, was performed. This time, there was only one bottom cell with a discharge, reducing the outlet area four times and thus increasing the vertical velocity four times, compared to Exp. 1. The vertical velocity of the discharge is still small and the process is still mainly buoyancy driven. The outlet was located at the grid cell specified by the indices (i,j) = (100,4).

7.1 Evolution of the marked basin water

Fig. 7.1 shows the evolution of $\frac{V_\gamma}{V_0}$ as a function of time. The three stages can also be identified here. The shape of the graph is similar to the one from Exp. 1, but the periods of the stages are not equal. Stage I lasts for a longer time than in the Exp.1, around 120 days, where the first approx. 100 days could fit an exponential decay model. Then follows a stagnation, Stage II, for about 40 days. Around day 160, the decay continues and Stage III can be identified.

Around day 62, half of the tracer water is lifted above 300 m depth. By the end of the simulation, about 70% of the tracer water is lifted above this area.

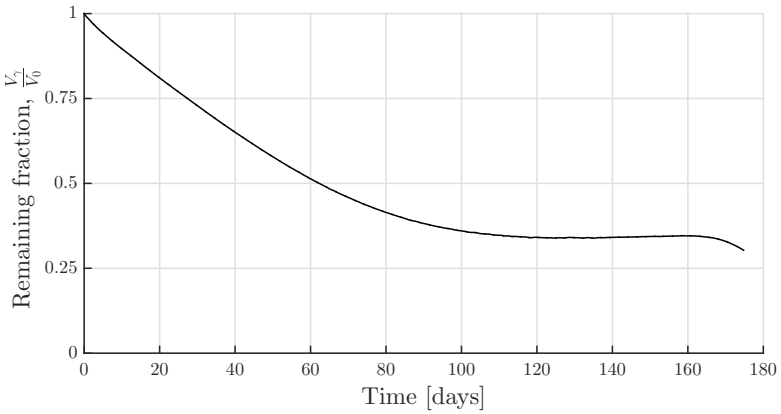

Fig. 7.1. The remaining fraction of marked bottom water below 300 m relative to its initial value, $\frac{V_\gamma}{V_0}$, plotted against time.

7.2 Evolution of the oxygen concentration

Fig. 7.2 shows how the concentration of dissolved oxygen varies through the simulation of 175 days. The solid line is the average concentration in the bottom 100 m of the basin, and the dashed line is the average concentration in the top 100 m. The results are similar to the same plot in Exp. 1, and will not be further discussed.

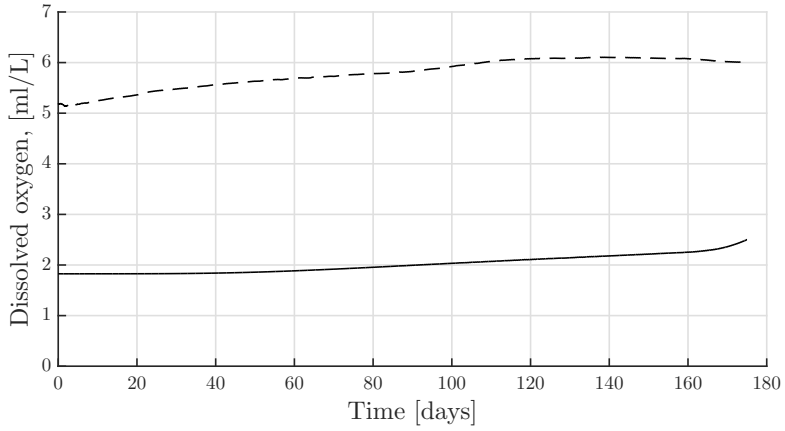

Fig. 7.2. The evolution of the average oxygen concentration below 300 m depth (solid line) and above 100 m depth (dashed line).

7.3 Concentration fields of the passive scalars

Fig. 7.3 shows the concentration fields of the dissolved oxygen and the tracer after 30, 100, 145 and 175 days of simulated time.

The evolution of the concentration fields is similar to those from Exp. 1. A difference is the amount of bottom water entrained into the buoyant plume. In Exp. 1, more of the basin water were entrained into the rising plume and thus removed from the bottom. In this experiment, the water in the bottom 25-50 m of the basin retains high/low concentrations of the tracer/dissolved oxygen for a longer time than in Exp. 1. Another difference is the terminal height of the plume. In this simulation, the plume is located a bit higher up than in Exp. 1.

7.4 Density

The velocity fields and the density distribution showed the same patterns with small variations, compared to the results from Exp. 1. Fig. 7.4, showing the density distribution after 30, 100, 145 and 175 days of simulation time, is included to illustrate the

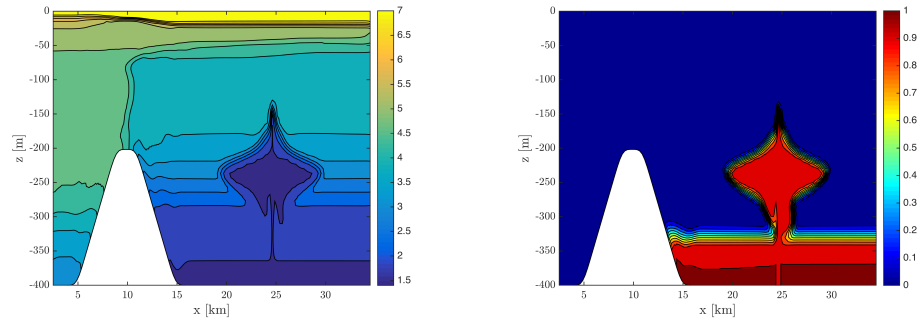

(a) Day 30.

(b) Day 30.

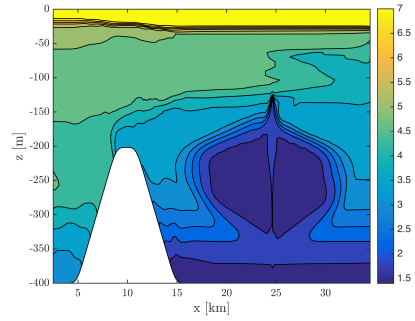

(c) Day 100.

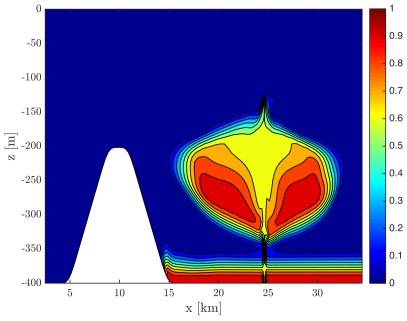

(d) Day 100.

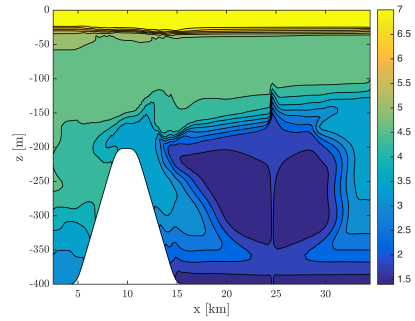

(e) Day 145.

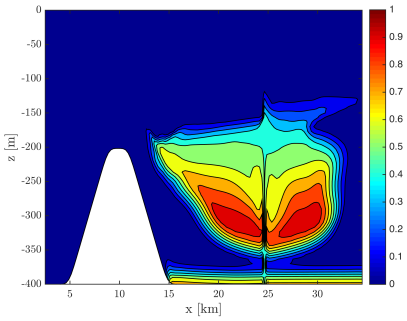

(f) Day 145.

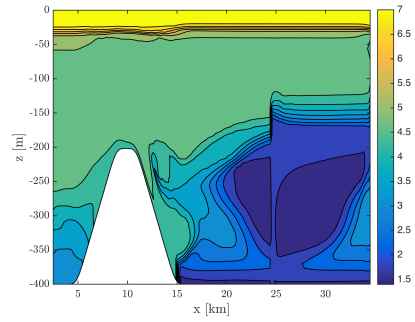

(g) Day 175.

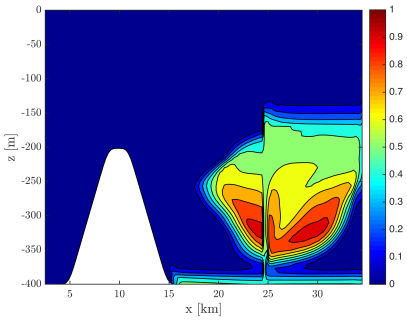

(h) Day 175.

Fig. 7.3. Contour of the dissolved oxygen [ml/L] (left column) and the passive tracer (right column) after 30 (a-b), 100 (c-d), 145 (e-f) and 175 (g-h) days of simulated time. The plane is a cross section through the y-directional centre.

similarities and differences. The evolution of the density distribution is similar to the one in Exp. 1, based on the isopycnals observed in the basin at various times. The disturbances of the isopycnals are seen at several of the same locations.

A clear difference is that the intrusion depth of the buoyant plume is higher up than in Exp. 1. The density of the buoyant plume is less than that in Exp. 1, indicating less entrainment of the denser basin water. This is what leads to the difference in the intrusion depth. A buoyant plume of lesser density will raise higher up towards the surface.

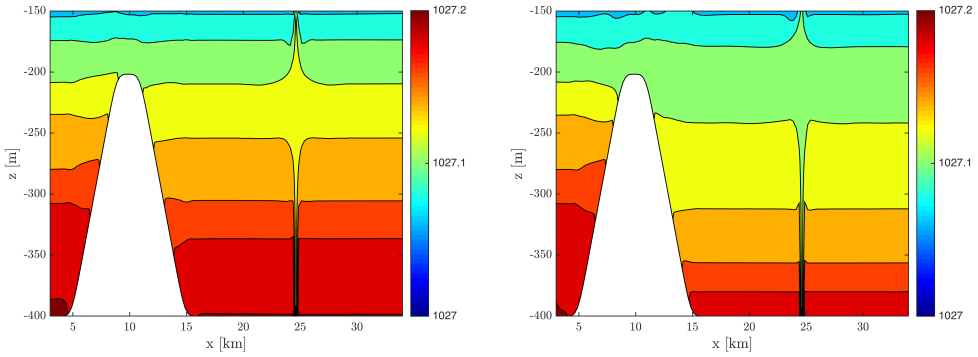

(a) Day 30.

(b) Day 100.

(c) Day 145.

(d) Day 175.

Fig. 7.4. Contour of the density, ρ [kg/m^3], at day 30, 100, 145 and 175, with a contour spacing of 0.02 kg/m^3. The upper 160 m is omitted to better illustrate the density differences in the basin and around the sill.

7.5 Discussion

Due to the similarities with Exp. 1, no further results from this experiment will be presented. Considering the small difference between this experiment and Exp. 1, the

similarities of the results indicates a robustness of the model and the set-ups.

The difference between the set-ups of the discharge in this experiment and Exp. 1, is a four times smaller discharge area in this experiment. The main observed difference between the results from this experiment and Exp. 1, are the intrusion depth of the buoyant plume and the entrainment of the bottom water. The area of discharge, for the same flux, determines how much of the ambient denser water is mixed with the fresh water. This again determines the density and hence the intrusion depth of the buoyant plume. An even smaller discharge area might lead to a intrusion depth higher up, at the cost of less mixing of the bottom water.

8. Exp. 4: One outlet of 2 m^3s^{-1}

Another experiment with a flux of 2 m^3s^{-1}, was performed. The discharge was released through one bottom cell. The outlet was located at the grid cell specified by the indices (i,j) = (100,4).

8.1 Evolution of the marked basin water

Fig. 8.1 shows $\frac{V_\gamma}{V_0}$ as a function of time. In this experiment as well, the decay rate varies in time. First, the slope of the decay is steep, and between day 60 to 120, it is reduced. An exponential decay model could fit the first 60-80 days, but then the slope is reduced and does not fit to a decay constant associated with the initial decay rate. A stagnation period, denoted as Stage II in the previous experiments, is not observed. However, there is a period of weak reduction between days 120 and 160. The derivative is never zero, even though it is close to zero in this period. Around day 160, the slope grows steeper again.

Even though there is no period of stagnation or increase in this experiment, three different stages can be identified. First, there is a period where an exponential decay model could fit the data, Stage I. Then follows a period of decay at a lower rate, Stage II, starting around day 80. Around day 165 a period of another of decay rate begins, Stage III.

After approx. 38 days, V_γ is halved compared to the initial value, V_0. By the end of the simulation, less than 13% of the original marked water remains below 300 m depth.

8.2 Evolution of the oxygen concentration

Fig. 8.2 shows the average concentration of dissolved oxygen in the area covering the top and bottom 100 m beyond the sill. In the top layer, the average concentration increases for the first 100-120 days and then seems to stabilise around a concentration of about 6 ml/L. The evolution in the top layer is similar to the one in Exp. 1 and Exp. 3.

In the depths, there is a continuous increase of the concentration, with a varying growth rate. By the end of the simulation, the average concentration below 300 m depth in the

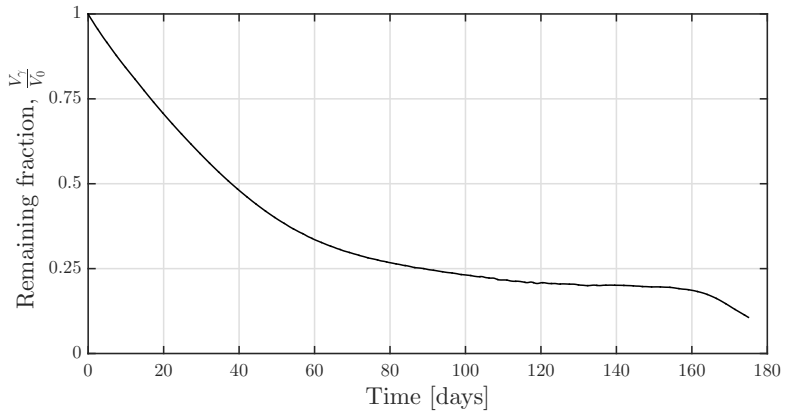

Fig. 8.1. The remaining fraction of marked bottom water below 300 m relative to its initial value, $\frac{V_\gamma}{V_0}$, plotted against time.

basin is close to 4 ml/L and does not seem to stagnate, since the growth is steepening from around day 165.

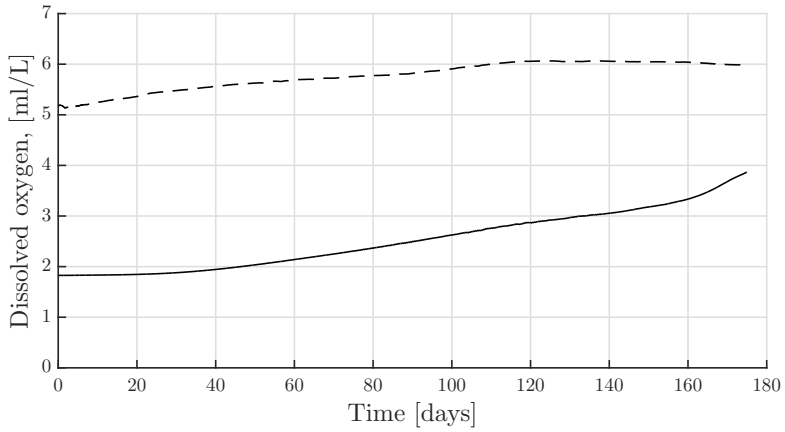

Fig. 8.2. The evolution of the average oxygen concentration below 300 m depth (solid line) and above 100 m depth (dashed line).

8.3 Concentration fields of the passive scalars

Fig. 8.3 shows the concentration fields of the dissolved oxygen and the tracer after 30, 70, 100 and 175 days of simulated time.

The plume rises and has a top point around 100 m depth. From day 30 trough day 70 to day 100, the width increases and more of the marked water is entrained. This is seen as the concentrations of the tracer near the bottom are reduced, and the concentrations of dissolved oxygen increases. At day 100, only low concentrations of the tracer is seen

at the bottom. The water with hypoxic concentrations of oxygen is no longer seen near the bottom, but is seen in parts of the plume/the elevated water. The plume spreads laterally between 150 m to 250 m depth. At day 100, the left side of the plume has been transported to the top of the sill, and the right side is near the eastern boundary. At day 175, only a relatively small area of high concentrations of the tracer visible, in the lower right corner of the basin. This is were the oxygen concentrations are lowest as well.

On the lower left side of the basin, the concentrations of dissolved oxygen are of the same contour level as the coastal water between 300 m to 200 m depth, a concentration ranging between 4 ml/L to 4.5 ml/L. There thus is a contrast between the left and right side of the bottom 300 m of the basin, regarding the concentrations of dissolved oxygen.

8.4 Velocity fields

Fig. 8.4 illustrates the horizontal and vertical velocity fields after 50 and 160 days of simulation. At day 50, there is an inflow over the sill, see Fig. 8.4a, resulting in positive vertical velocities on the left side of the sill and negative vertical velocities on the right side, see Fig. 8.4b. A convergence towards the outlet area and an area of lateral divergence between 150 m to 250 m depth are seen in Fig. 8.4a.

At day 160, in Fig. 8.4c, the convergence towards the outlet area is seen as well. Along the sill, there are positive horizontal velocities. They are visible along the right side of the sill and down into the basin, where they continue on the basin floor for a few km. In combination with the negative vertical velocity at this day, seen in Fig. 8.4d, this implies an inflow of water all the way down to the bottom of the basin. There might be a high-density intrusion, and the density distribution can be used to evaluate this further.

8.5 Density distribution

Fig. 8.5 illustrates the density distribution below 100 m depth after 30, 100, 160 and 175 days of simulation.

The evolution of the density distribution through time is similar to the other experiments. The density of the basin water is reduced in time, and thus provide conditions for high-density intrusion. At day 100, 160 and 175, in Fig. 8.5 (c-d), isopycnals seen as nearly horizontal lines on the outside of the sill gradually bends down along the right

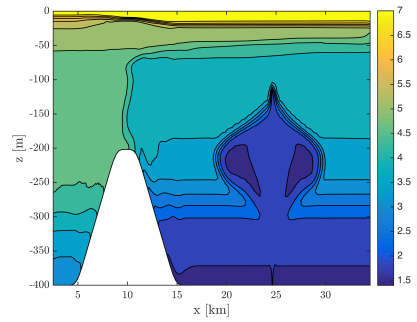

(a) Day 30.

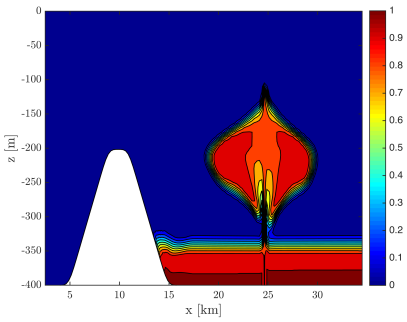

(b) Day 30.

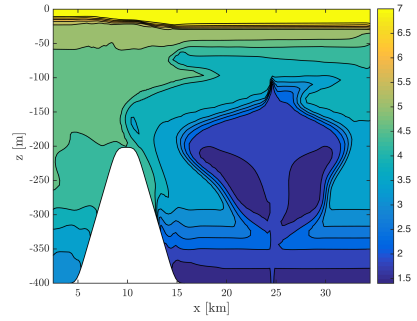

(c) Day 70.

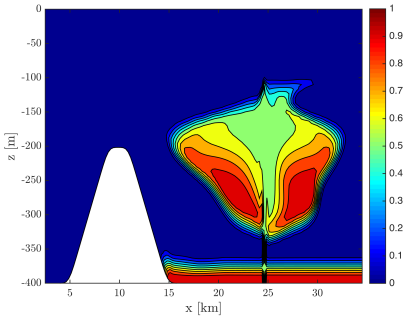

(d) Day 70.

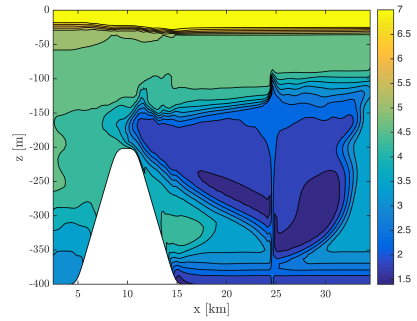

(e) Day 100.

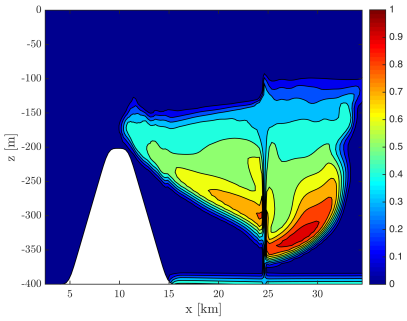

(f) Day 100.

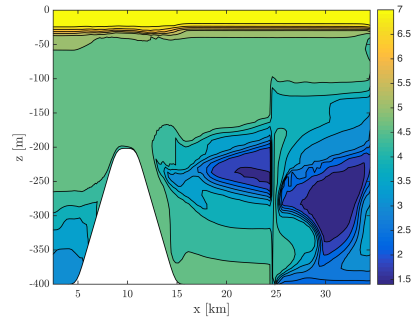

(g) Day 175.

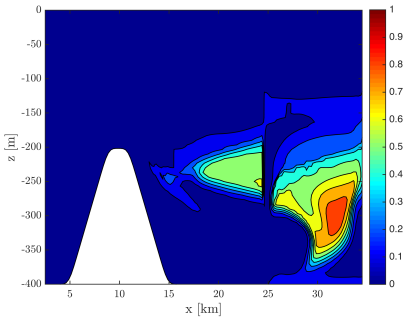

(h) Day 175.

Fig. 8.3. Contour of the dissolved oxygen [ml/L] (left column) and the passive tracer (right column) after 30 (a-b), 70 (c-d), 125 (e-f) and 175 (g-h) days of simulated time. The plane is a cross section through the y-directional centre.

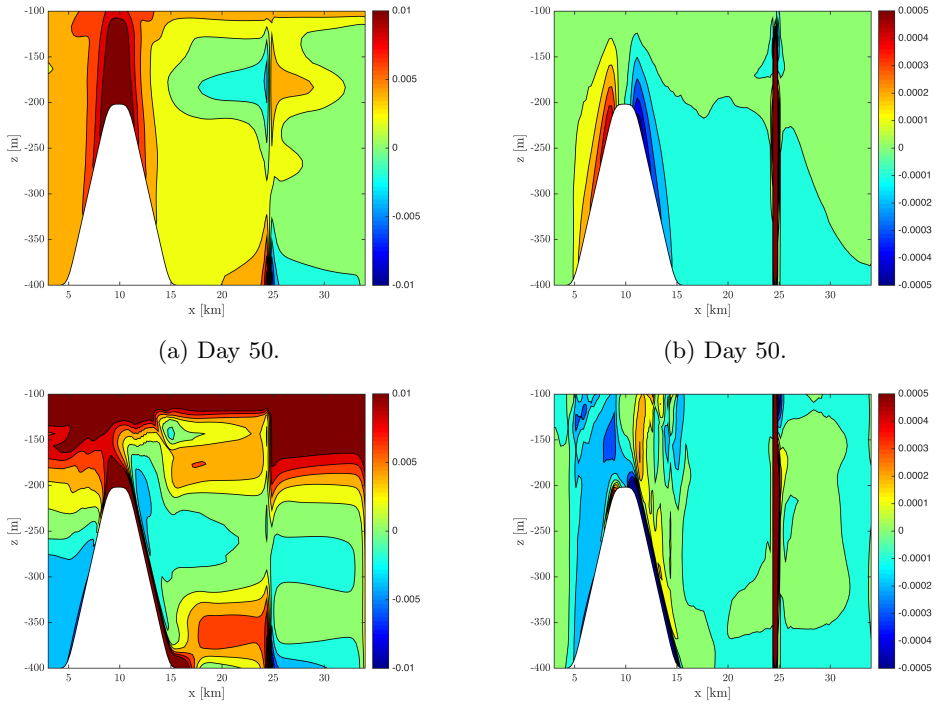

(a) Day 50.

(b) Day 50.

(c) Day 160.

(d) Day 160.

Fig. 8.4. Contour of the horizontal velocity component, U [ms^{-1}] (left column), and the vertical velocity component, W [ms^{-1}] (right column). The contour spacings are $2 \cdot 10^{-3}$ ms^{-1} for U and $1 \cdot 10^{-4}$ ms^{-1} for W.

side of the sill. This can be interpreted as water of greater density flowing over the sill and down to a depth where it intrudes. At day 175, the density intrusion seem to reach a depth near the bottom of the basin, as the isopycnal follows the slope down to approx. 375 m depth before it bends horizontally.

Disturbances in the isopycnals are seen, and evolves in time. At day 30, in Fig. 8.5a, there is a peak where the buoyant plume is decelerated by negative buoyancy. This peak is also seen at day 100, but in another isopycnal, of lower density. At day 100, disturbances are also seen in other isopycnals and other areas of the fjord, especially above the sill. In time, disturbances of greater amplitude and in other areas are seen in several isopycnals. In particular, disturbances are seen along the right side of the sill and on the right side of the buoyant plume.

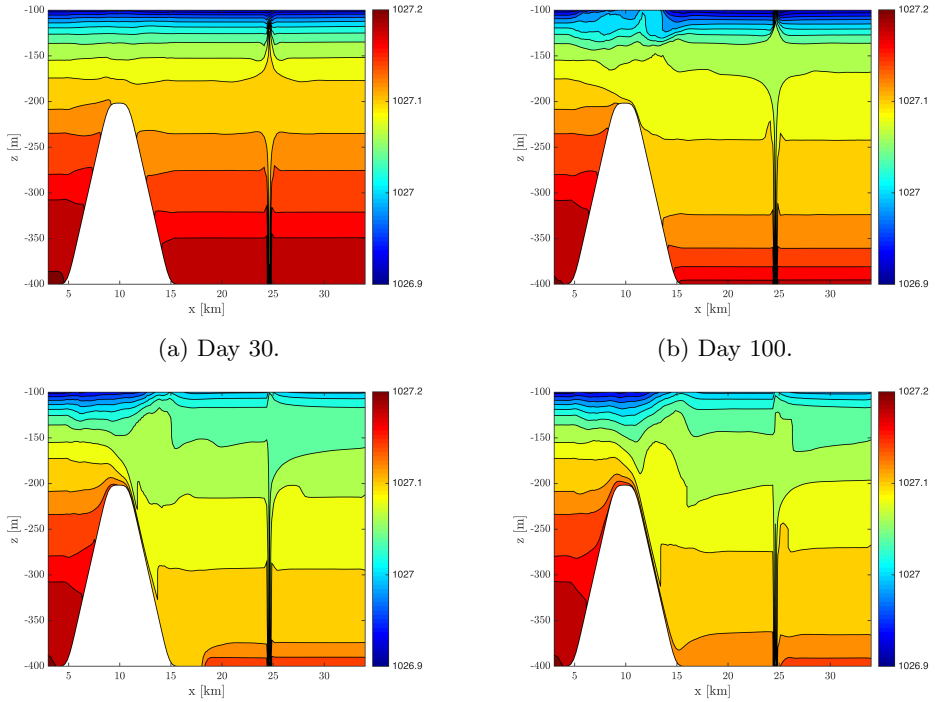

(a) Day 30.

(b) Day 100.

(c) Day 160.

(d) Day 175.

Fig. 8.5. Contour of the density, ρ [kg/m^3], at day 30, 100, 160 and 175, with a contour spacing of 0.02 kg/m^3. The upper 100 m is omitted to better illustrate the density differences near sill depth.

8.6 Turbulent vertical mixing

Fig. 8.6 shows the vertical eddy diffusion coefficient, K_H, at day 100 and 160. At day 100, the values above the outlet cell, represented by the dotted line, are greater than

the minimum value up to a depth of 125 m. Above the two neighbouring grid cells, the dashed and solid line, the value of K_H is at the minimum value except for the top 25 m. This pattern is observed in results from other experiments, and is assumed to be caused by the estaurine circulation caused by the river.

At day 160, the dotted line is similar to the one at day 100. Above the two neighbouring grid cells, K_H has larger values between 100 m and 200 m depth. This indicates that the turbulence kinetic energy is produced also in the neighbouring area of the discharge, at this time.

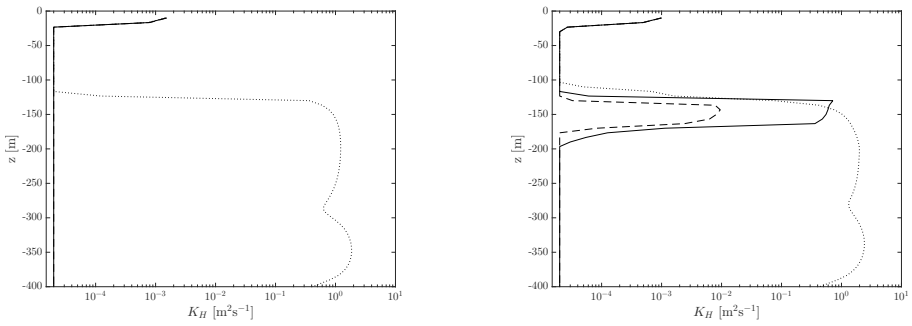

(a) Day 100. (b) Day 160.

Fig. 8.6. The vertical variation of the vertical eddy diffusion coefficient, K_H [m^{2}s^{-1}], plotted on a log-scale at day 100 and day 160. Data is collected from vertical lines where the j-coordinate is 4 and the i-coordinate is 100 (dotted line), 101 (solid line) and 102 (dashed line).

Fig. 8.7 shows the areas where the Richardson number has critical values (red areas). At day 30, only a column above the discharge is seen, as well as a wider area near the top of this column, around 175 m depth. The same column is seen at day 100, but it now ends at a depth between 125 m to 150 m. An area at around 100 m depth, to the right of the sills location, is also observed. In the isopycnals from the same time, disturbances in this area was seen. At the right side of the sill, between 250 m and 300 m depth, a minor area of critical Ri number is visible.

At day 160 and day 175, there are critical Ri numbers in more areas, and they cover a larger area as well. The column above the discharge ends at approx. 150 m depth, and to the right side of the ending point, there is an area of possible unstable water masses, as the Ri number is below its critical value. Along the sill, there are areas of critical Ri number. There is also an area to the right of the sill, located between 150 m to 200 m depth at day 160, and between 175 m to 225 m at day 175. These are all areas where disturbances in the isopycnals were seen, indicating that these are unstable water masses.

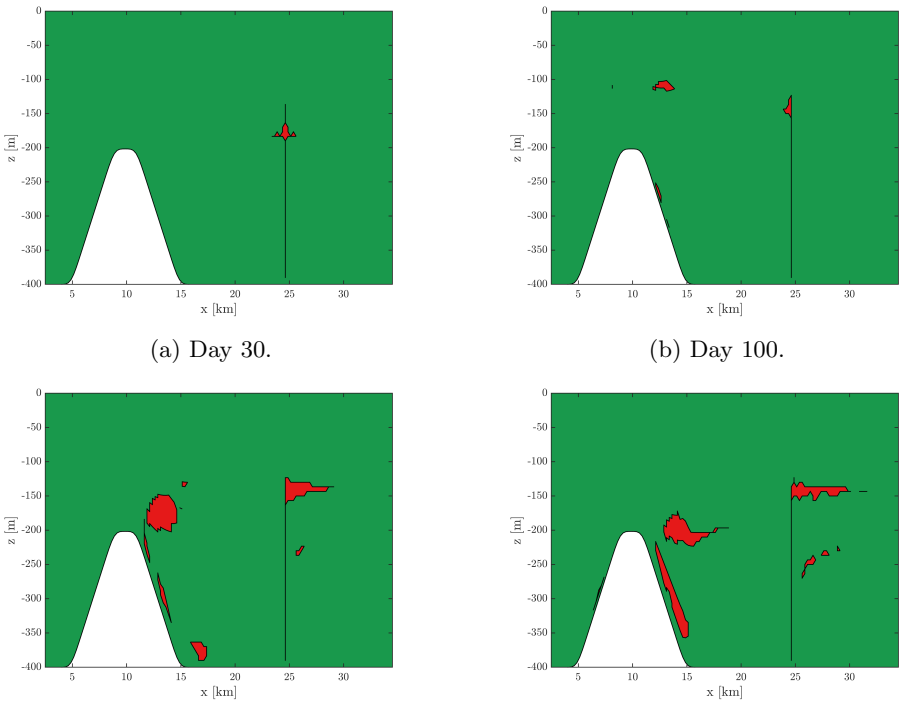

(a) Day 30.

(b) Day 100.

(c) Day 160.

(d) Day 175.

Fig. 8.7. Areas where the Richardson number is below (red) and above (green) its critical value, 0.25, through days 30, 100, 145 and 175.

8.7 Discussion

Three periods of decay with various decay rates could be identified in the results from this experiment. In Stage I an exponential decay model could fit the data. This decay is gradually reduced until Stage II, which in this experiment was not a stagnant period, but a period of weaker decay. This implies that the tracer flux out of the bottom 300 m of the basin are greater than the tracer flux into the bottom 300 m of the basin, for all times of the simulation. It also implies that the balance between the tracer flux into and out of the basin varies, since the decay rate varies. The increased decay in Stage III, indicates that the tracer flux into the bottom 300 m of the basin has been reduced compared to the tracer flux out of this area. The intrusion of coastal water could explain the reduction in the tracer flux into the depths of the basin.

If compared with Exp. 3, this experiment illustrates the effect of doubling the fresh water discharge flux. It resulted in a shorter halving time of the marked bottom water, 38 days in this experiment versus 62 days in Exp. 3. In this experiment, some of the basin water are transported out of the basin. This is seen in the figures showing the concentration fields at day 100 and 175, where the plume of the water originally below 300 m were stretched out over the sill. This was not observed in the results from Exp. 3.

In this experiment and Exp. 3, for the first 100 days, there are still concentrations of the tracer visible at the bottom. This was not the case in Exp. 1 and Exp. 2, indicating a greater amount of entrainment in those experiments compared to Exp. 3 and Exp. 4.

The coastal water intrudes and brings more saturated water into the depths. The intruding water is more saturated than coastal water at greater depths, and thus greatly increases the oxygen concentrations in the depths. This was seen in the concentration field of dissolved oxygen at day 175, where coastal water with a dissolved oxygen concentration of 4-4.5 ml/L intrudes down into the basin.

9. Discussion

This thesis has used the three-dimensional numerical ocean model, BOM, to estimate effects of a submerged fresh water discharge in a threshold fjord. Threshold fjords are characterized by low concentrations of oxygen in the depths of the basin caused by weak and/or infrequent exchange of the basin water.

The principle of discharging fresh water at a depth and thus creating artificial upwelling is known to give promising results for the primary production. The aim of the present study was to examine if a discharge at the bottom of the basin could increase the ventilation of the fjord and hence increase the concentration of dissolved oxygen in the basin.

In the previous chapters, the preliminary and the four main experiments were described and discussed. In the four experiments, the discharge area and flux were adjusted. Exp. 1 and Exp. 2 were executed to examine the effect of increasing the discharge flux greatly, from 1 m^3s^{-1} to 10 m^3s^{-1}. The discharge area of these two experiments was equal. The discharge flux in Exp. 3 was equal to the one of Exp. 1, but the discharge area was four times reduced. By doing so, the sensitivity of the numerical model to the discharge area could be investigated. In Exp. 4, the discharge area was equal to that of Exp. 3 but a doubling of the discharge flux in order to investigate the effect of this parameter was done.

The following sections aim to highlight the main findings and discuss possible implications.

The three stages

Three periods denoted as Stage I, Stage II and Stage III were identified in the graphs showing the time-evolution of the marked basin water, V_γ. These stages were all found in all the experiments, but lasted for different periods of time. The three stages are determined by the flux of the tracer out of and into the bottom 300 m of the basin.

In Stage I, a decay of V_γ is seen in all experiments, but with varying decay rates. As the vertical velocity fields have shown, there is a downward velocity on both sides of the rising plume. This is to replace the water that is entrained and elevated by the

discharge. In the beginning, the inflowing water has a tracer concentration of zero. This implies that the flux of the tracer into the bottom 300 m of the basin is zero as well. The decay rate in the beginning of each experiments thus reflects the flux of the tracer out of the bottom 300 m of the basin. An exponential decay model fits the evolution of V_γ for a period, but it does not fit when the tracer water flows back to the basin.

For an exponential decay model, the half-life $T_{\frac{1}{2}}$, can be used as a time scale of the decay. In the preliminary experiments, the half-life was estimated to approx. 2-4 years, dependent on the simulation time. In contrast, the half-life based on a time series from Stage I in the four main experiments, was estimated to 10 to 70 days, dependent on the experiment. Even though the decay was reduced after Stage I, these are clear improvements of the half-life estimated by the preliminary experiments.

In Stage II, the decay rate was reduced, and in one experiment it turned into a period of growth. In the transition from Stage I to Stage II, the tracer flux into the area below 300 m gradually increases. The water descending on both sides of the discharge will in time bring the tracer back into the bottom area, below 300 m. From the figures showing the density distribution at various times, we saw that water masses originally located farther up in the basin descended downwards as the denser water, at and near the bottom, was entrained by the buoyant plume. Stage II of growth/stagnation was barely visible in Exp. 4, but clearly observed in the three other experiments. This implies that the tracer flux out is always greater than the tracer flux into area below 300 m, in Exp. 4. In Exp. 2, a period of growth was observed, suggesting a greater tracer flux into the area below 300 m compared to the flux out of this area.

The flux of the tracer back into the bottom 300 m of the basin decreases with time, and a transition into Stage III starts. The density on the outside of the sill are nearly constant through time, because of the forced inflow boundary condition (FRS) of salinity and temperature. However, the density of the basin is reduced in time because of the entrainment and elevation of the dense water by the buoyant plume. This will in time set the required conditions for exchange by high-density intrusion. It is interesting to notice that the transition to Stage III for all experiments coincide with i) positive horizontal velocities and negative vertical velocities along the right side of the sill and ii) isopycnals with origin at sill depth, bending along the right side of the sill and following the sill down into the basin. These two observations are evidence for high-density intrusion, and Stage III might thus be connected to those events.

Area of discharge

The grid resolution determines the minimum discharge area, which in this experiment was restricted to a relatively large area. Nevertheless, the size of the discharge area was investigated; a large area and a four times larger area.

Exp. 1 and Exp. 3 can be compared to evaluate the effect of the area of discharge. In each experiment, the intrusion depth varied with time, approximately over a 50 m to 100 m range, because the density distribution in the basin varied in time. In Exp. 3, the buoyant plume generally reached a greater height than in Exp. 1. The results from these two experiments suggests that a larger discharge area results in intrusion at a greater depth. The intrusion depth of the plume is determined by the density of the rising plume in combination with the density distribution in the basin. This implies that a larger discharge area results in a higher density of the buoyant plume, which is caused by a greater amount of entrainment.

The large discharge area in these simulations could be compared to placing a correspondingly large plate above the discharge and let the fresh water through small holes in this plate, called a diffuser plate. Another way to enhance the mixing could be to place the discharge beneath a large plate and let the water flow out and over the plate. This has been done before to enhance entrainment (McClimans et al., 2010).

The discharge flux

Three various discharge fluxes have been applied, 1, 2 and 10 m^3s^{-1}. It has been stated that in Stage I, when halving time occurred, the decay of V_γ reflects the tracer flux out of the bottom 300 m area, as the flux into this area is zero in this stage. Experiments with the same discharge area, but with different discharge fluxes can be compared to evaluate the effect of the discharge flux on the halving time.

Table 9.1 illustrates the half-life estimated by the four main experiments. We see that the increase of the discharge flux by a factor ten gives a reduction in the half-life by a factor seven, comparing Exp. 1 and Exp. 2. Comparing Exp. 3 and Exp. 4, we see that a doubling of the discharge flux gives a reduction in the half-life by a factor of 1.6.

Based on these two comparisons, it is hard to state a general connection between the discharge flux and the half-life. The area of discharge also have an impact on the half-life, as there is a difference between the halving times from Exp. 1 and Exp. 3, which have the same discharge flux. However, the results from this study implies that an

Discharge area	Exp.	Flux [m^3s^{-1}]	$T_{\frac{1}{2}}$ [days]
$4\Delta x\Delta y$	1	1	70
	2	10	10
$\Delta x\Delta y$	3	1	62
	4	2	38

Table 9.1. The half-life $T_{\frac{1}{2}}$ based on a times series from Stage I for the four main experiments.

increase of the discharge flux reduces the half-life of the deepest portion of the basin water.

Remarks

In the modelling process, many choices must be taken and assumptions are made. Some remarks regarding this will be presented.

Only one basin was included in the model of the fjord. In reality, a fjord arm can consist of many basins of various depths through its length. The focus of this study was to examine the effect of a fresh water submerged discharge in a basin, and thus one idealized basin was chosen.

The concentration fields, and all other figures used, was based on data taken from the vertical plane through the y-directional centre. It was assumed that, since the Coriolis force was neglected, there would be a symmetry around this vertical plane.

Wind was not included in the model. In reality, this has an effect on the exchange across the sill. Both strong winds locally, but also winds along the coast which can induce internal Kelvin waves which propagate along the coast and subsequently into fjords (Kundu et al., 2016).

The river runoff was assumed constant in these experiments. In reality, the river runoff varies and is large when the snow melts or when the precipitation/rainfall is high. This also neglects seasonal variations of fjord circulation. The surface current induced by the river would probably not have a great effect on the circulation of the basin water. However, if fresh water from the rivers are to be utilised as a submerged discharge, the constant flux applied in these experiments might be hard to sustain all year round. It might be that the actual flux would be time-varying by the seasonal changes. This might give other results, but is not possible to predict based on the experiments performed in this study.

The set-ups of utilising the river water as a source of the submerged discharge is proposed in Berntsen et al. (2002): Placing a dam with surface level a few meters above the fjords surface level can provide the required potential energy to drive the river water down to a submerged discharge.

If the fresh water should be discharged through a pipe with a diameter of for instance 1 m, there would be a lower density of the rising plume due to less entrainment. This would bring the entrained water higher up, but less basin water would be mixed into the blend. It is desired to have a large entrainment of the basin water, and in particular the hypoxic water, in order to dilute this by the fresh, well-saturated water. However, the plume should rise to a depth where the water is easier exchanged by the tidal. A large entrainment results in a higher density of the plume, and thus intrusion at a greater depth.

Conclusions and further work

Based on this model and its assumptions, some conclusions can be drawn. It is clear that a submerged discharge, as modelled in this study, would increase the ventilation and circulation of the basin water. Both the value of the discharge flux and the area of the discharge has an impact on the amount of entrainment and the terminal height of the rising plume, and thus the time scale of the ventilation.

In all four experiments with a submerged fresh water discharge, the density of the basin water was reduced. This effect of the submerged discharge sets the system in a state susceptible for high-density intrusion. Combined with seasonal variations, such as inflow of denser coastal water by surges, this could potentially result in a greater exchange of the basin water. Modelling of a seasonal varying open boundary condition will be a natural extension of the present study.

If further work on investigating this subject has promising results, and the project is put to life, this could also be beneficial for the ecosystems in the fjords. Not only is the concentrations of dissolved oxygen in the basin raised, but a positive side effect could be an enhancement in the primary production, as artificial upwelling of the basin water most likely brings nutritious water up to the productive, euphotic zone. A drawback could be if the upwelling brings toxic hydrogen sulphide towards the surface. It should also be considered that areas where there normally are higher concentrations of dissolved oxygen experiences hypoxia for shorter periods when the bottom water is entrained and elevated. Both these factors could cause poor living conditions for periods of time. The

real life impact of this is uncertain, however it might be beneficial to promote a more gradual exchange of the basin water in order to account for these possible effects.

Further studies of this model set-up could include an adjustment of the grid size near the discharge, to mimic a more realistic size of the discharge area. It could also include adjustments of the mixing coefficients to simulate the effect of less entrainment which is comparable to a reduced discharge area.

The Coriolis force was neglected because it is a usual assumption for narrow fjords. For further work, it might be considered to include a Coriolis force to examine its potential effect.

A. List of symbols

Symbol	Description
U	Velocity component in the x-direction
V	Velocity component in the y-direction
W	Velocity component in the z-direction
η	Surface elevation
H	Bottom static depth
P	Pressure
T	Temperature
S	Salinity
ρ	In situ density
ρ_0	Reference density
g	Gravity
f	The Coriolis parameter
K_M	Vertical eddy viscosity
A_M	Horizontal eddy viscosity
K_H	Vertical eddy diffusivity
A_H	Horizontal eddy diffusivity
γ	The tracer used for marking the bottom water
V_0	The initial volume of the marked water below 300 m depth
V_γ	The volume of the marked water remaining below 300 m depth
$T_{\frac{1}{2}}$	The half-life of the marked basin water
λ	Decay constant in exp. decay model
O_2	Dissolved oxygen
O_{2A}	The average concentration of O_2 in the upper 100 m of the fjord
O_{2B}	The average concentration of O_2 in the lower 100 m of the basin

See Section 2.3-2.4 for description of the parameters involved in the boundary conditions and the turbulence closure scheme.

References

Aarre, E., Andersson, A., Lambrechts, L., & Eriksen, A. G. (2016). *Den syke fjorden.* `https://www.bt.no/nyheter/lokalt/i/5WV1K/Den-syke-fjorden`. Bergens Tidende. (Accessed 03-11-2017)

Aksnes, D. L., Aure, J., Johansen, P.-O., Johnsen, G. H., & Salvanes, A. G. V. (n.d.). Multi-decadal warming and associated decline in dissolved oxygen of deep fjord basins.
(In preparation)

Aure, J., & Stigebrandt, A. (1989). On the influence of topographic factors upon the oxygen consumption rate in sill basins of fjords. *Estuarine, Coastal and Shelf Science*, *28*(1), 59–69.

Aure, J., Strand, Ø., Erga, S. R., & Strohmeier, T. (2007). Primary production enhancement by artificial upwelling in a western norwegian fjord. *Marine Ecology Progress Series*, *352*, 39–52.

Berntsen, J. (2004). *Users guide for a modesplit σ-coordinate numerical ocean model* (Tech. Rep.). Dept. of Applied Mathematics, University of Bergen, Johs. Bruns gt. 12, N-5008 Bergen, Norway.

Berntsen, J., Aksnes, D. L., & Foldvik, A. (2002). Production enhancement by artificial upwelling: a simulation study. In O. Vadstein & Y. Olsen (Eds.), *Sustainable Increase of Marine Harvesting: Fundamental Mechanisms and New Concepts* (pp. 177–190). Springer.

Blumberg, A. F., & Mellor, G. L. (1987). A description of a three-dimensional coastal ocean circulation model. *Three-dimensional coastal ocean models*, 1–16.

Breitburg, D., Levin, L. A., Oschlies, A., Grégoire, M., Chavez, F. P., Conley, D. J., ... Zhang, J. (2018). Declining oxygen in the global ocean and coastal waters. *Science (New York, N.Y.)*, *359*(6371), eaam7240.

Cushman-Roisin, B., & Beckers, J.-M. (2011). *Introduction to Geophysical Fluid Dynamics: Physical and Numerical aspects.* San Diego: Elsevier Science.

Durski, S. M., Glenn, S. M., & Haidvogel, D. B. (2004). Vertical mixing schemes in the coastal ocean: Comparison of the level 2.5 Mellor-Yamada scheme with an enhanced version of the K profile parameterization. *Journal of Geophysical Research: Oceans*, *109*(C1).

Fischer, H. B., List, J. E., Koh, C. R., Imberger, J., & Brooks, N. H. (1979). *Mixing in Inland and Coastal Waters.* New York: Academic Press.

Gill, A. E. (1982). *Atmosphere-ocean dynamics (international geophysics series)* (Vol. 30). New York: Academic Press.

Haidvogel, D. B., & Beckmann, A. (1999). *Numerical Ocean Circulation Modeling.* Imperial College Press, London.

Haltiner, G. J., & Williams, R. T. (1980). *Numerical Prediction and Dynamic Meteorology* (2nd ed.). New York: Wiley.

Johansen, P.-O., Isaksen, T. E., Bye-Ingebrigtsen, E., Haave, M., Dahlgren, T. G., Kvalø, S. E., ... Rapp, H. T. (2018). Temporal changes in benthic macrofauna on the west coast of norway resulting from human activities. *Marine pollution bulletin*, *128*, 483–495.

Kantha, L. H., & Clayson, C. A. (2000). Tides and Tidal Modeling. In *Numerical models of oceans and oceanic processes* (Vol. 66, pp. 375–492). Elsevier.

Kundu, P. K., Cohen, I. M., & Dowling, D. R. (2016). *Fluid Mechanics* (6th ed.). Elsevier, Oxford.

Liseth, P. (1977). *Dykket utslipp i resipient: utledning og fortynning av avløpsvann* (Vol. 14). Prosjektkomiteen for rensing av avløpsvann: i kommisjon hos Liv Jansen, NIVA.

Liungman, O., Rydberg, L., & Göransson, C.-G. (2001). Modeling and observations of deep water renewal and entrainment in a Swedish sill fjord. *Journal of Physical Oceanography*, *31*(12), 3401-3420.

Malin, M. (1989). Analysis of turbulent forced plumes into a stable environment. *Applied mathematical modelling*, *13*(2), 122–126.

Martinsen, E. A., & Engedahl, H. (1987). Implementation and testing of a lateral boundary scheme as an open boundary condition in a barotropic ocean model. *Coastal engineering*, *11*(5-6), 603–627.

Maruyama, S., Tsubaki, K., Taira, K., & Sakai, S. (2004). Artificial upwelling of deep seawater using the perpetual salt fountain for cultivation of ocean desert. *Journal of oceanography*, *60*(3), 563–568.

McClimans, T., Handå, A., Fredheim, A., Lien, E., & Reitan, K. (2010). Controlled artificial upwelling in a fjord to stimulate non-toxic algae. *Aquacultural Engineering*, *42*(3), 140–147.

Mellor, G. L., Ezer, T., & Oey, L.-Y. (1994). The pressure gradient conundrum of sigma coordinate ocean models. *Journal of atmospheric and oceanic technology*, *11*(4), 1126–1134.

Mellor, G. L., & Yamada, T. (1982). Development of a turbulence closure model for geophysical fluid problems. *Reviews of Geophysics*, *20*(4), 851–875.

Mesinger, F., & Arakawa, A. (1976). Numerical methods used in atmospheric models.

Phillips, N. A. (1957). A coordinate system having some special advantages for numerical forecasting. *Journal of Meteorology*, *14*(2), 184–185.

Røed, L., & Cooper, C. (1986). Open boundary conditions in numerical ocean models. In J. J. O'Brien (Ed.), *Advanced physical oceanographic numerical modelling* (pp. 411–436). Springer.

Schmidtko, S., Stramma, L., & Visbeck, M. (2017). Decline in global oceanic oxygen content during the past five decades. *Nature*, *542*(7641), 335-339.

Shapiro, R. (1975). Linear filtering. *Mathematics of computation*, *29*(132), 1094–1097.

Smagorinsky, J. (1963). General circulation experiments with the primitive equations: I. The basic experiment. *Monthly weather review*, *91*(3), 99–164.

Soltveit, T., & Jensen, P. M. (2017). *Bunnvannet i Masfjorden måskiftes ut mener HI-forskere.* `https://kyst.no/article/bunnvannet-i-masfjorden-maa-skiftes-ut-mener-hi-forskere/`. (Accessed 09-02-2018)

Strand, Ø., Strohmeier, T., Aure, J., Asplin, L., Grefsrud, E., & Husa, V. (2014). Kontrollert oppstrømning av næringsrikt dypere vann i fjorder. In S. Andersen (Ed.), *Karbonfangst og matproduksjon i fjorder* (pp. 93–129). Havforskningsinstituttet.

Sverdrup, H. U., Johnson, M. W., Fleming, R. H., et al. (1942). *The oceans: Their physics, chemistry, and general biology.* Englewood Cliffs, New York: Prentice-Hall.

Trujillo, A. P., & Thurman, H. V. (2017). *Essentials of oceanography* (12. ed.). Boston: Pearson.

Turner, J. (1969). Buoyant plumes and thermals. *Annual Review of Fluid Mechanics*, *1*(1), 29–44.

Wang, D.-P. (1984). Mutual intrusion of a gravity current and density front formation. *Journal of Physical Oceanography*, *14*(7), 1191–1199.

Wolanski, E. (2015). *Estuarine ecohydrology: an introduction* (1st ed.). Amsterdam: Elsevier.